

MICROSCOPIC ANALYSIS OF ELASTIC AND INELASTIC PROTON SCATTERING FROM ^{12}C

L. RIKUS, K. NAKANO and H. V. VON GERAMB[†]

Theoretische Kernphysik, Universität Hamburg, Luruper Chaussee 149, 2000 Hamburg 50, W. Germany

Received 1 September 1983

Abstract: First-principle optical potentials and DW inelastic transition amplitudes to the $J^\pi = 1^+$, $T = 0, 1$ states of ^{12}C are studied using an energy- and density-dependent nuclear matter reaction matrix as effective interaction which is based on the Paris potential. The analysis covers existing data for angular distributions of differential cross sections, polarizations, analysing powers, polarization and analysing power differences and spin-flip probabilities between 122 and 400 MeV. We stress in this work the capabilities of calculations involving no adjustable parameters. The calculations presented herein are a case study and status report of proton-nucleus scattering at medium energies.

1. Introduction

Microscopic studies of intermediate-energy proton scattering are a central theme in the investigation using recently installed accelerators in the 100 to 400 MeV region. Such studies illuminate nuclear structure deep inside the nucleus together with aspects of the hadronic interaction mediating the scattering¹⁾. In this energy régime it is known that the NN reaction cross section has a wide minimum and therefore nuclear transparency is at a maximum²⁾. In addition at these energies the effects of pion production are still minimal, nevertheless it is expected that elastic and inelastic scattering should be basically explainable within a direct reaction picture which knows only of nucleons, although certain mesonic degrees of freedom may occur. The unconfirmed conjecture over critical opalescence³⁾ confirms this view that the explicit mesonic effects are difficult to isolate. Excitation of nuclear isobars, in particular the $\Delta(3,3)$ resonance, is feasible and such excitations could behave like doorway states resulting in collective enhancement/quenching in Gamow-Teller transitions⁴⁾. Along this line developments of the microscopic optical potentials of nonrelativistic or relativistic origin provide evidence that interference effects between low and high momentum transfer mechanisms are crucial at intermediate energies⁵⁾.

[†] Supported by Bundesministerium für Forschung und Technologie, Contract 06HH746 and NATO grant no. 279.81.

The microscopic understanding of medium- to high-energy elastic scattering has made great progress⁵⁾. At high energy, approaches based on multiple scattering theory⁶⁾ use the free NN scattering amplitude as a driving operator on the elementary NN level. In the most commonly used approximation⁷⁾, the scattering mechanism is assumed to be a coherent superposition of elementary NN interactions in which the rest of the target nucleons play the role of spectators preserving the c.m. motion. The validity of this idea has been verified for energies above 500 MeV [ref.⁸⁾] and has led to many high precision measurements of nuclear matter distributions around 0.8 and 1 GeV. For energies below 500 MeV the scattering of two nucleons is influenced more and more by the phase-space limitations imposed by the surrounding nucleons. Quantitatively this effect may be observed in the overestimation of reaction cross sections within KMT using the free *t*-matrix⁹⁾.

Medium-energy proton scattering between 100 and 400 MeV has the advantage that it lies in the energy region of maximum transparency but has the disadvantage that many-body effects complicate the reaction picture. Thereby we distinguish between phase-space limitations of the two-nucleon interaction due to the surrounding fermion medium leading to Pauli blocking, off-shell effects in the NN scattering and higher-order effects including excitation of intermediate states in the target system leading to the necessity of coupled-channels calculations. In the list of many-body effects Pauli blocking is preponderant. Dispersion effects, however, assume great significance with decreasing energy. Altogether the medium effects yield corrections in cross sections of up to 50 % at 100 MeV. In this context it is understandable that a sophisticated effective interaction is the central theme for nucleon scattering at such energies. The introduction of complex energy- and density-dependent interactions with all the complications of spin/isospin dependence has proved essential for quantitatively explaining data¹⁰⁾.

The underlying direct reaction picture suggests the concept of an interaction zone. To be less specific we take it as nuclear matter describable in terms of a non-interacting Fermi gas in its ground state. Thus any given point in the nucleus is characterized by a local Fermi momentum. In computing the effective interaction this nuclear matter approach¹¹⁻¹⁴⁾ provides the realm in which all practical calculations can be performed without relying on further approximations referring to a particular nucleus. Recent emphasis on full relativistic treatments¹⁵⁾ of the many-body problem at various levels of sophistication for elastic and inelastic scattering cause us to expect that the now classic non-relativistic treatment presented herein will be superseded in the near future. This new approach will ultimately combine the microscopic understanding of nuclear forces on the level of QCD with the relativistic many-fermion theory.

The aim of the present work is to give a status report of a fully microscopic calculation from first principles for elastic and inelastic scattering with a nuclear matter reaction matrix as driving transition operator introduced as a complex

energy- and density-dependent effective interaction. All applications will be limited to proton scattering from ^{12}C in the energy range 122 MeV to 400 MeV. As input for the reaction matrix we use the momentum-dependent Paris potential¹⁶⁾ which is hitherto considered the best semi-phenomenological potential available. In particular, we intend a study of the reliability and limitations of the microscopic optical potential in its ability to reproduce differential cross sections and analyzing powers. This study must be seen together with several phenomenological attempts to explain these same data^{17,18)}.

The inelastic studies are limited to the isoscalar and isovector spin-flip transitions ($J^\pi, T = 1^+, 0$ (12.71 MeV) and $J^\pi, T = 1^+, 1$ (15.11 MeV)) in ^{12}C . From these two transitions we expect a sensitive test of the non-central force components, in particular the tensor force which is otherwise of little importance in the optical model or in normal-parity transitions.

The two inelastic transitions chosen have been studied extensively at various energies in the past emphasizing different aspects. To mention a few of them, the inelastic transitions to these states are associated with a rather large cross section and rather modest energy resolution is sufficient for experiment. The isovector transition has been of particular interest in attempts to ascertain the presence of pion condensation²¹⁾. A rich sample of data is available: differential cross sections at 122, 155, 200, 398 MeV, analyzing power data at 122, 200 and 398 MeV, spin-flip probabilities for the substate populations at 200 MeV and the difference between polarization and analyzing power at 155 MeV. All of these data have been previously analyzed¹⁸⁾ under various aspects and in particular with the application of a free NN scattering amplitude generated by Love and Franey²²⁾.

In the present analysis we make extensive use of the reaction matrix. Optical model potentials containing complex central and spin-orbit potentials are generated within a folding model approach. The inelastic transitions are analyzed in the framework of the DWBA in which the transition operator is identified with the t -matrix and the required distorted waves are generated with the microscopic optical potential. The structure information required about the target nucleus stems from elastic scattering for the ground-state density and Cohen-Kurath's²³⁾ shell-model wave functions for the transition amplitudes. It is most unfortunate that the known limitations in these wave functions will restrict the conclusions that can be drawn from the analyses presented here but a viable alternative with such a rich sample of data does not exist. Inelastic electron scattering analyses lend support to our claims.

In the next section we present the salient features entering into the reaction matrix calculations and how the effective interaction based thereon was generated. In sect. 3 elastic scattering results together with the expressions for the underlying folding model are presented. Various features of the microscopic optical potentials as compared to phenomenological results are discussed. Data comparisons comprise differential cross section and polarization data with momentum

transfer < 1200 MeV/c. Predictions are also made for 250, 300 and 350 MeV to bridge the gap between the experimental results and to show the steady energy variation of the observables. In sect. 4 inelastic scattering studies to the isovector and isoscalar spin-flip states are presented and put in perspective with results from previous analyses. In sect. 5 a brief summary and conclusions can be found.

2. Theoretical background

The theoretical background of the microscopic optical potential follows the infinite nuclear matter approach which was initiated by H fner and Mahaux¹¹⁾ and has been reviewed and applied by several other authors¹²⁾. This approach identifies the single-particle mass operator with the optical model in infinite nuclear matter in the lowest order of the hole-line expansion

$$U_{\text{opt}}(\mathbf{a}) = \sum_{|\mathbf{m}| < k_F} \langle \phi_{a,m} | t(\omega) | \phi_{a,m} \rangle_A; \quad (1)$$

$t(\omega)$ in the antisymmetrized plane wave matrix element satisfies the Bethe-Goldstone equation (BG)

$$t(\omega) = V + V G_Q^{(+)}(\omega) t(\omega), \quad (2)$$

wherein V is the free NN Paris potential¹⁶⁾. The Green function $G_Q^{(+)}(\omega)$ contains outgoing wave boundary conditions and medium effects such as the requirement of propagation in unoccupied intermediate states under the influence of an average potential acting on the single particles:

$$G_Q^{(+)}(\omega) = \sum_{|\mathbf{b}|, |\mathbf{c}| > k_F} \frac{|\phi_{b,c}\rangle \langle \phi_{b,c}|}{\omega - e(b) - e(c) + i\epsilon}. \quad (3)$$

We further identify the starting energy as the sum of the projectile energy $e(a)$ and the energy of the struck single particle in the medium:

$$\omega = e(a) + e(m). \quad (4)$$

There are a number of methods available to compute the matrix elements of eq. (1). Since the techniques for the solution of wave equations are well known one introduces, with the identity

$$\langle \phi_{a,m} | t(\omega) | \phi_{a,m} \rangle = \langle \phi_{a,m} | V | \psi_{a,m} \rangle, \quad (5)$$

the correlated wave function $\psi_{a,m}$ satisfying a related BG equation

$$\psi_{a,m} = \phi_{a,m} + G_Q^{(+)}(\omega) V \psi_{a,m}. \quad (6)$$

To obtain the matrix elements, eq. (5), one may either solve for $t(\omega)$ or ψ . We solve eq. (6) in coordinate representation for the correlated wave function with the standard matrix techniques for Fredholm integral equations of the second kind.

To summarize salient features of the procedure, we introduce c.m. and relative coordinates:

$$\begin{aligned} \mathbf{K} &= \mathbf{k}_a + \mathbf{k}_m = \mathbf{k}_b + \mathbf{k}_c, \\ \mathbf{R} &= \frac{1}{2}(\mathbf{r}_a + \mathbf{r}_m) = \frac{1}{2}(\mathbf{r}_b + \mathbf{r}_c), \\ \mathbf{k} &= \frac{1}{2}(\mathbf{k}_a - \mathbf{k}_m), \\ \mathbf{q} &= \frac{1}{2}(\mathbf{k}_b - \mathbf{k}_c), \\ \mathbf{r} &= \mathbf{r}_a - \mathbf{r}_m = \mathbf{r}_b - \mathbf{r}_c. \end{aligned} \quad (7)$$

All wave functions are decomposed into partial waves and classified with respect to good total spin/isospin channels. The Pauli projection function

$$Q(\mathbf{K}, \mathbf{q}, k_F) = |\mathbf{b}, \mathbf{c}\rangle \langle \mathbf{b}, \mathbf{c}|, \quad (8)$$

where $|\mathbf{b}\rangle, |\mathbf{c}\rangle > k_F$, ensures that the two particles in the intermediate states propagate only in unoccupied momentum states above the Fermi momentum k_F . This distinguishes various momentum regions:

$$Q(\mathbf{K}, \mathbf{q}, k_F) = Q(\mathbf{K}, \mathbf{q}, k_F) \begin{cases} = 0 & \text{for } \frac{1}{4}K^2 + q^2 < k_F^2 \\ = 1 & \text{for } |\frac{1}{2}K - q| > k_F. \end{cases} \quad (9)$$

For all other momenta we use the spherical average:

$$\begin{aligned} Q(\mathbf{K}, \mathbf{q}, k_F) &= \frac{1}{2} \int_{-1}^1 dx Q(\mathbf{K}, \mathbf{q}, k_F) \\ &= \int_0^{(\frac{1}{4}K^2 + q^2 - k_F^2)/Kq} dx \\ &= (\frac{1}{4}K^2 + q^2 - k_F^2)/Kq. \end{aligned} \quad (10)$$

The single particle energies $e(k)$, eqs. (3) and (4), in the propagator contain the kinetic energy and a self-consistent energy-dependent potential energy:

$$e(k) = \frac{\hbar^2 k^2}{2m} + U(k). \quad (11)$$

Various restrictions and analytic and/or numerical choices of this potential energy

result in different forms of t -matrix elements representing alternative levels of approximation. The ultimate choice for $U(k)$ is the fully self-consistent complex mass operator itself but due to the numerical complexities involved it has never been used. For the calculations described herein the real part of the lowest order nuclear matter mass operator as defined by eq. (1) was used. In addition the self-consistency process which was initiated with the choice $U(k) = 0$ was only taken to one iteration. For energies above 100 MeV this is a rather good approximation to the final result since the key effect there stems from Pauli blocking. For lower energies more iterations are necessary to achieve self-consistency. The enormous amount of computer time required is, however, daunting. Note that when $k_F = 0$, $U(k) = 0$ the Pauli function goes over to one and the resulting matrix elements are those of the free t -matrix which can be directly compared with experimental NN data.

In addition to replacing the numerator of the kernel function $G_Q^{(+)}(K, k, q, k_F)$ by the spherically averaged Pauli function of eq. (10) the energy denominator is replaced by the spherical average defined by

$$\begin{aligned}
 & e(a) + e(m) - e(b) - e(c) \\
 &= \frac{\hbar^2}{m} (k^2 - q^2) + U(|\tfrac{1}{2}\mathbf{K} + \mathbf{k}|) + U(|\tfrac{1}{2}\mathbf{K} - \mathbf{k}|) \\
 &\quad - U(|\tfrac{1}{2}\mathbf{K} + \mathbf{q}|) - U(|\tfrac{1}{2}\mathbf{K} - \mathbf{q}|) \\
 &= \frac{\hbar^2}{m} (k^2 - q^2) + \frac{\int_{-1}^1 \{U(|\tfrac{1}{2}\mathbf{K} + \mathbf{k}|) + U(|\tfrac{1}{2}\mathbf{K} - \mathbf{k}|)\} Q(\mathbf{K}, \mathbf{k}, k_F) dx}{\int_{-1}^1 Q(\mathbf{K}, \mathbf{k}, k_F) dx} \\
 &\quad - \frac{\int_{-1}^1 \{U(|\tfrac{1}{2}\mathbf{K} + \mathbf{q}|) + U(|\tfrac{1}{2}\mathbf{K} - \mathbf{q}|)\} Q(\mathbf{K}, \mathbf{q}, k_F) dx}{\int_{-1}^1 Q(\mathbf{K}, \mathbf{q}, k_F) dx}. \tag{12}
 \end{aligned}$$

The integrals defined in eq. (12) are performed numerically using gaussian quadrature with a minimal number of points ($n = 3,5$) for simplicity.

The resulting equation is transformed into a system of linear equations by replacing the integral by a trapezoidal rule integration. The equation is solved with the partial waves $J \leq 10$ in coordinate space with 60 points of 0.035 fm and 40 points of 0.2 fm step size. By defining standing wave boundary conditions the problem is reduced to a purely real one. The Green function is numerically Fourier transformed.

The correlated wave functions which are the solutions of eq. (6) then enable us

to generate a complex energy- and density-dependent effective interaction in the form of a two-nucleon potential

$$\begin{aligned} t(r) &= \sum_{ST} t_0^{ST}(r) P^S P^T + \sum_T t_1^T(r) \mathbf{L} \cdot \mathbf{S} + \sum_T t_2^T(r) S_{12} \\ &= \sum_k (R_k \cdot S_k), \end{aligned} \quad (13)$$

using the prescription proposed by Siemens²⁵). With the scalar product we distinguish tensor operators R_k , of rank k , acting on coordinate space elements and S_k acting in spin (isospin) space, respectively.

The tensor amplitudes are obtained with

$$\begin{aligned} \langle L \| R_k \| L \rangle \langle ST \| S_k \| ST \rangle &= \sum_J \hat{k} \hat{J} (-)^{J-L-S} (\hat{T})^{\frac{1}{2}} \left\{ \begin{matrix} L & S & J \\ S & L & k \end{matrix} \right\} \\ &\times (LSJT | t | LSJT), \end{aligned} \quad (14)$$

with t -matrix elements computed with the correlated two-body wave functions

$$\begin{aligned} &(LSJT | t(\mathbf{k}, \mathbf{k}) | LSJT) \\ &= \frac{\sum_{L'} \int_{|\mathbf{p}| \leq k_F} d^3 p j_L(\frac{1}{2}|\mathbf{k}-\mathbf{p}|r) V_{LL'}^{J,ST}(r) u_{L'L'}^{J,ST}(r, k_F, \mathbf{k}, \mathbf{p})}{\int_{|\mathbf{p}| \leq k_F} d^3 p j_L(\frac{1}{2}|\mathbf{k}-\mathbf{p}|r) j_{L'}(\frac{1}{2}|\mathbf{k}-\mathbf{p}|r)}. \end{aligned} \quad (15)$$

$V_{LL'}^{J,ST}(r)$ are the two-body NN potential radial form factors of the Paris potential in the channel $(J, ST; LL')$.

The central component $S_0 = P^S \cdot P^T$ and

$$R_0 = R_0^{(LL,ST)} = \frac{\sum_J \hat{J} (LSJT | t | LSJT)}{\hat{S} \hat{L}}. \quad (16)$$

The spin-orbit components $S_1 = \frac{1}{2}(\boldsymbol{\sigma}_1 + \boldsymbol{\sigma}_2) \cdot \mathbf{P}^T$ and

$$R_1 = R_1^{(LL,T)} \cdot \mathbf{L} = \frac{\sum_J \hat{J} \langle \mathbf{L} \cdot \mathbf{S} \rangle (L1JT | t | L1JT)}{2\hat{L}L(L+1)} \mathbf{L}. \quad (17)$$

The tensor components, $S_2 = [\boldsymbol{\sigma}_1 \times \boldsymbol{\sigma}_2]_2 \cdot \mathbf{P}^T$ and

$$\begin{aligned} R_2 &= 3\sqrt{\frac{8}{15}\pi} R_2^{(LL',T)} Y_2(\hat{\mathbf{r}}) \\ &= \sqrt{5\pi} \frac{\sum_J \hat{J} (-)^{J+1} (L1JT | t | L1JT) \left\{ \begin{matrix} L & \frac{1}{2} & J \\ 1 & L & 2 \end{matrix} \right\}}{\langle LL'00 | 20 \rangle \sqrt{\hat{L} \hat{L}}} Y_2(\hat{\mathbf{r}}). \end{aligned} \quad (18)$$

The l -dependence is eliminated with averaging between plane-wave states. This yields for the central interaction

$$t_0^{ST}(r) = \frac{\sum_{L \geq 0} \varepsilon(L+S+T+1) \hat{L} R_0^{(LL,ST)} W_{LL}(r)}{\sum_{L \geq 0} \varepsilon(L+S+T+1) \hat{L} W_{LL}(r)}, \quad (19)$$

the spin-orbit interaction

$$\begin{aligned} t_1^T(r) = & \frac{1}{3} \frac{\sum_{L \geq 1} \varepsilon(L+T) L(2L+3) R_1^{(LL,T)}(r) W_{LL}(r)}{\sum_{L \geq 1} \varepsilon(L+T) L(2L+3) W_{LL}(r)} \\ & + \frac{1}{3} \frac{\sum_{L \geq 1} \varepsilon(L+T) \hat{L} R_1^{(LL,T)}(r) W_{LL}(r)}{\sum_{L \geq 1} \varepsilon(L+T) \hat{L} W_{LL}(r)} \\ & + \frac{1}{3} \frac{\sum_{L \geq 1} \varepsilon(L+T)(L+1)(2L-1) R_1^{(LL,T)}(r) W_{LL}(r)}{\sum_{L \geq 1} \varepsilon(L+T)(L+1)(2L-1) W_{LL}(r)}, \end{aligned}$$

and the tensor interaction

$$t_2^T(r) = \frac{\sum_{L \neq L'} \varepsilon(L+T) \sqrt{\hat{L} \hat{L}'} \hat{J} \langle LL00|20 \rangle \{ \begin{smallmatrix} L & 1 & J \\ 1 & L' & 2 \end{smallmatrix} \} R_2^{(LL',T)}(r) W_{LL'}(r)}{\sum_{L \neq L'} \varepsilon(L+T) \sqrt{\hat{L} \hat{L}'} \hat{J} \langle LL00|20 \rangle \{ \begin{smallmatrix} L & 1 & J \\ 1 & L' & 2 \end{smallmatrix} \} W_{LL'}(r)}, \quad (21)$$

with the notation

$$\varepsilon(n) = \begin{cases} 0, & n \text{ odd} \\ 1, & n \text{ even}, \end{cases} \quad (22)$$

$$W_{LL'} = \int_{|p| \leq k_F} d^3 p j_L(\frac{1}{2}|k-p|r) j_{L'}(\frac{1}{2}|k-p|r). \quad (23)$$

For applications it is necessary to parametrize the above potential in terms of Yukawa's. To assure an optimal representation we Fourier transform $t(r)$ into momentum space and apply a χ^2 fitting. This procedure permits us to put emphasis on the physically significant momentum region and cut off the poorly understood momentum regions. The momentum space Yukawa expressions are:

$$\text{central} \quad t_0^{ST}(k) = \sum_{i=1}^4 \frac{4\pi t_i^{ST}}{\mu_i^2 + k^2}, \quad (24)$$

$$\text{spin-orbit} \quad t_1^T(k) = \sum_{i=1}^4 4\pi t_i^{LS,T} \left\{ \frac{1}{k^2} \tan^{-1} \left(\frac{k}{\mu_i} \right) - \frac{\mu_i}{k(k^2 + \mu_i^2)} \right\}, \quad (25)$$

$$\text{tensor} \quad t_2^T(k) = \sum_{i=1}^4 \frac{32\pi k^2 t_i^{TN,T}}{(k^2 + \mu_i^2)^3}. \quad (26)$$

The mass parameters μ_i (inverse ranges) are *a priori* fixed to cover the range contained in the free NN interaction. The potential strength parameters V_i are uniquely obtained by minimizing

$$\chi^2 = \int_0^{5 \text{ fm}^{-1}} \{t(k) - t_a(k)\}^2 dk. \quad (27)$$

The r -space representation of the effective interaction is easily obtained by back transformation and is of the form:

$$\text{central} \quad t_0^{ST}(r) = \sum_{i=1}^4 t_i^{ST} \frac{e^{-\mu_i r}}{r}, \quad (28)$$

$$\text{spin-orbit} \quad t_1^T(r)(\mathbf{L} \cdot \mathbf{S}) = \sum_{i=1}^4 t_i^T \frac{e^{-\mu_i r}}{r} (\mathbf{L} \cdot \frac{1}{2}(\boldsymbol{\sigma}_1 + \boldsymbol{\sigma}_2)), \quad (29)$$

$$\text{tensor} \quad t_2^T(r)S_{12} = \sum_{i=1}^4 t_i^T r^2 \frac{e^{-\mu_i r}}{r} \left(\frac{3(\boldsymbol{\sigma}_1 \cdot \mathbf{r})(\boldsymbol{\sigma}_2 \cdot \mathbf{r})}{r^2} - (\boldsymbol{\sigma}_1 \cdot \boldsymbol{\sigma}_2) \right). \quad (30)$$

Tables of this effective interaction are given in ref.²⁰⁾.

3. Elastic scattering

Accurate scattering data from ^{12}C have recently been measured at Indiana University (IUCF) at 122, 160 [ref.¹⁷⁾] and 200 [ref.¹⁸⁾] MeV. These data cover an angular region up to 160° and therefore represent a momentum transfer study up to 1200 MeV/c. Other data from the Upsala group at 180²⁶⁾ MeV and Los Alamos at 398 [ref.²⁷⁾] MeV are available in a more restricted angular region. However, the data comprises of angular distributions for differential cross sections and polarizations. This situation is quite unique and represents a challenge to optical model calculations with the nuclear ground-state properties known from recent high-precision electron scattering measurements up to 600 [ref.²⁸⁾] MeV/c. At the present level we are primarily concerned with the study of the local non-relativistic form of the optical potential which has been used previously²⁹⁾. This microscopic optical potential is obtained by folding the single-particle density[†] of

[†] The matter density function for ^{12}C from ref.¹⁷⁾ was used in all the calculations herein.

the target ground state with the complex effective interaction :

$$\begin{aligned}
 U(\mathbf{r}, E) = & \int d^2s \rho(|\mathbf{r} + \mathbf{s}|) \left\{ Z t_p^D(s, \hat{k}, E) + N t_n^D(s, \hat{k}, E) \right\} \\
 & + \int d^3s \rho(|\mathbf{r} + \frac{1}{2}\mathbf{s}|) \frac{3 j_1(\hat{k}s)}{k s} j_0(k(r)s) \\
 & \times \{ Z t_p^{EX}(s, \hat{k}, E) + N t_n^{EX}(s, \hat{k}, E) \}, \quad (31)
 \end{aligned}$$

wherein

$$\hat{k} = k_F(|\mathbf{r} + \frac{1}{2}\mathbf{s}|), \quad k_F(r) = [\frac{3}{2}\pi^2 \rho(r)]^{\frac{1}{3}}, \quad (32)$$

and the complex local momentum is given (self-consistently) by

$$\hbar k(r) = \sqrt{2m(E - U(r) - V_{\text{Coul}}(r))}. \quad (33)$$

The linear combinations of the nuclear matter central interaction t_0^{ST} required are given by

$$\begin{aligned}
 t_p^{D,EX} &= \frac{1}{4}(t_0^{01} \pm 3t_0^{11}), \\
 t_n^{D,EX} &= \frac{1}{8}(3t_0^{10} + t_0^{01} \pm t_0^{00} \pm 3t_0^{11}). \quad (34)
 \end{aligned}$$

In this equation ST refers to the two-body spin-isospin channels in which the effective interaction matrix elements are developed. The spin-orbit potentials are computed in a manner equivalent to that of Scheerbaum and Brieva and Rook³⁰):

$$\begin{aligned}
 U_{LS}(r, E) = & -\frac{1}{3}\pi \left[F_p(\rho_p(r), E) \frac{1}{r} \frac{\partial \rho_p(r)}{\partial r} \right. \\
 & \left. + F_n(\rho_n(r), E) \frac{1}{r} \frac{\partial \rho_n(r)}{\partial r} \right] \mathbf{l} \cdot \boldsymbol{\sigma}, \\
 F_p(\rho_p(r), E) = & \int t_{LS}^1(s, \rho_p(r), E) \left\{ s + \frac{3}{k(r)} j_1(k(r)s) \right\} s^3 ds, \\
 F_n(\rho_n(r), E) = & \frac{1}{2} \int \left[t_{LS}^1(s, \rho_n(r), E) \left\{ s + \frac{3}{k(r)} j_1(k(r)s) \right\} \right. \\
 & \left. + t_{LS}^0(s, \rho_n(r), E) \left\{ s - \frac{3}{k(r)} j_1(k(r)s) \right\} \right] s^3 ds.
 \end{aligned}$$

The effective interaction is taken to be the one within the interaction zone. This

prescription, generally known as the local-density approximation (LDA), is not unique since the interaction has a finite range and projectile and target nucleon coordinates refer to different density points in the medium.

These microscopic optical potentials have been calculated between 122 MeV and 400 MeV with the experimental charge density distribution as input. The real part is shown in fig. 1, displaying a strong energy dependence in the form factor. Microscopically this feature can be interpreted in different ways. Mahaux *et al.*¹⁹⁾ attribute the structural changes to the density dependence of the interaction. In the phenomenological Dirac approach³¹⁾ a balance between the vector and scalar field form factors is claimed to be responsible. Within the present context of the folding model the destructive interference of direct and knock-out exchange amplitudes has been shown to yield the above-mentioned effect. In brief our arguments are: Low momentum components correspond to large radial dimensions in coordinate space, i.e. the nuclear surface region is dominated by the singlet-even and triplet-even attractive low momentum part of the interaction. Both components become repulsive for momentum transfers > 350 MeV/c. The knock-on exchange part of the OMP samples the NN interaction around the incident momentum k which means that for energies above 60 MeV the exchange mechanism yields repulsive contributions to the real OMP. With ever-increasing energy this repulsion begins to dominate and we obtain an energy-dependent form-factor structure as shown in fig. 1. It is our understanding that the interplay between low momentum transfer direct amplitudes and high momentum exchange amplitudes are crucial. The density dependence of the interaction enhances this feature even at high energy as shown in fig. 2. A more detailed discussion of these arguments can be found in ref.²⁰⁾.

A comparison of the microscopic potentials based on the Paris potential as input in contrast to the Hamada-Johnson potential [see fig. 5c of ref.¹⁷⁾] shows that the bottle-shaped structure is more damped for the Paris potential. This is in agreement with the phenomenological findings but still leaves differences in detail. In particular the strong variation of the geometric parameters quoted in the analysis is only partly confirmed microscopically. The latter displays significantly less energy dependence. The intrinsic limitations of the double Woods-Saxon (DWS) parametrization¹⁷⁾ are likely to cause the uncertainty between strength and geometric parameters claimed. Perhaps the most crucial difference is seen in the behaviour of the real potential inside a radius of about 1 fm.

Beyond a momentum transfer of 600 MeV/c the experimental electron scattering density is unknown. For 200 MeV data this means that any analysis beyond 60° should start to deteriorate, a feature which is known³¹⁾ and confirmed herein. In coordinate space this means that the optical potential within $R < 1$ fm determines this large-angle scattering region. This dimension is comparable to the nucleon dimensions and we expect the very fine details of the short-range correlations to be extremely important in reproducing the experimental situation and therefore

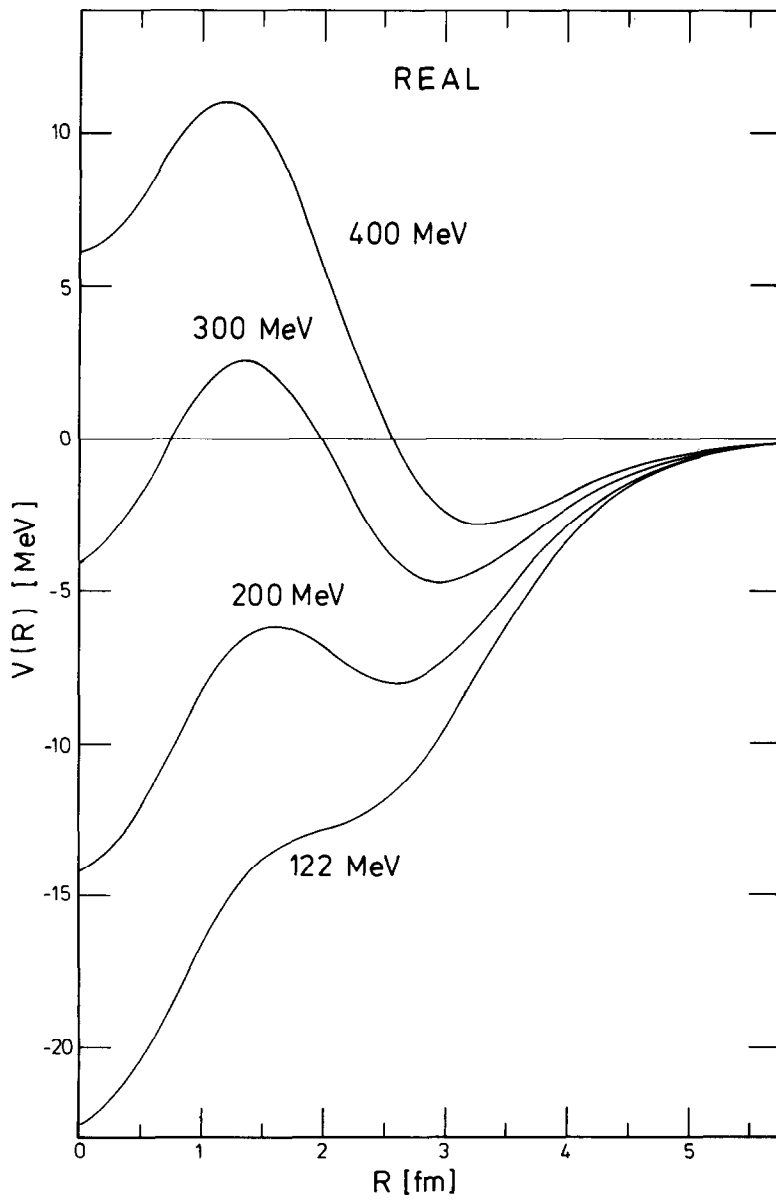


Fig. 1. The energy variation of the real part of the microscopic proton optical potential for scattering from ^{12}C .

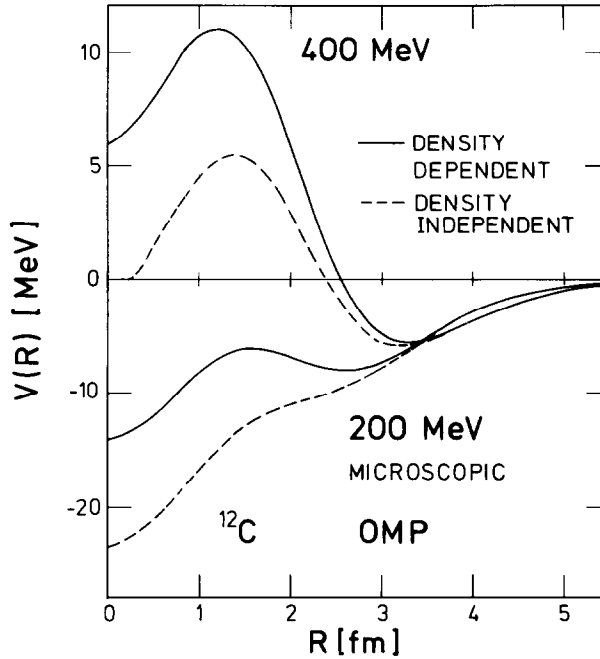


Fig. 2. The real part of the microscopic optical potential at 400 and 200 MeV. The full curves correspond to a folding calculation with the fully density-dependent t -matrix while the dashed curves were calculated using the free t -matrix (i.e. the $k_F = 0$ t -matrix).

should ultimately be included. The microscopic optical potential starts to break down beyond 900 MeV/c. At the present stage we have no way to attribute this failure to any definite cause.

The imaginary part of the optical potential increases practically linearly with energy. In fig. 3 we display the 200 MeV form factor with an insertion showing the energy variation of the strength in the centre, $W(R=0)$. From a first glance it appears that significant differences to the phenomenological potentials exist. The diffuseness of the imaginary potential, $a_W \approx 1$ fm, is significantly larger than values known from phenomenological potentials, $a_W \approx 0.6$ fm. The imaginary microscopic optical potential has volume integrals comparable to the standard parametrization but lies 40 % above the DWS. These are summarized in table 1. The microscopically computed reaction cross sections are around 260 mb whereas experimental values are at typically 225 mb [ref. ¹⁷]. This suggests the need for a renormalization of the strength of the imaginary potential due to non-locality effects. In practice this correction is complicated by the density dependence of the effective mass. In simple terms, for the central value of the imaginary potential the non-locality correction yields a reduction of 15 % as compared to the results

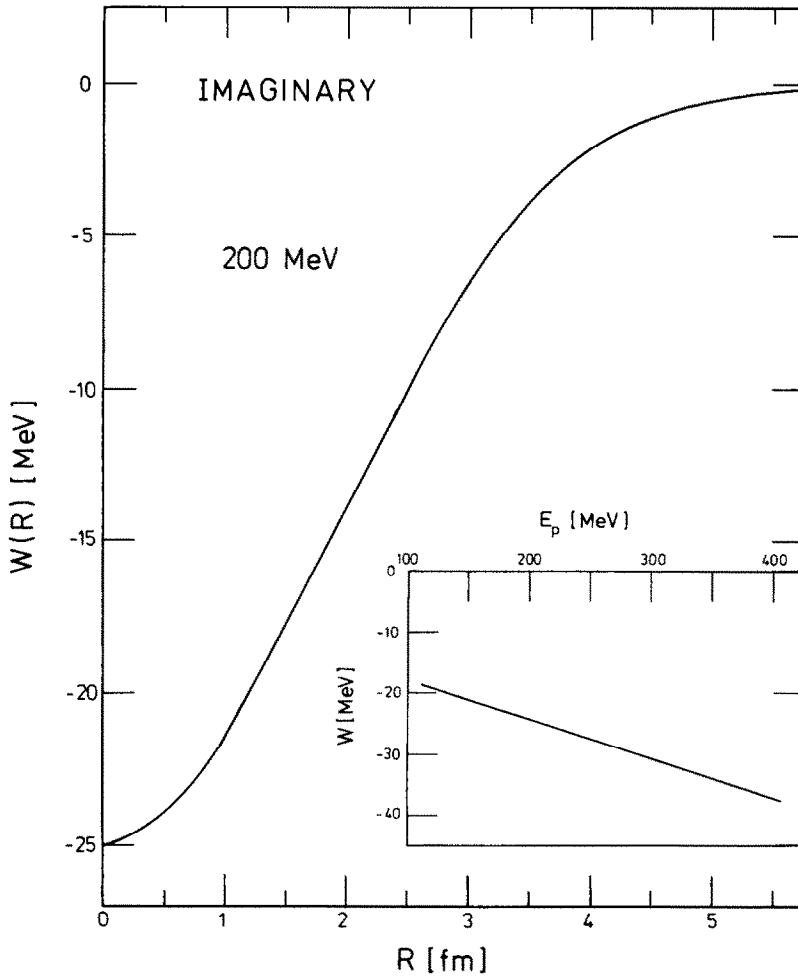


Fig. 3. The imaginary part of the 200 MeV microscopic optical potential. The insert shows the energy variation of the strength at the centre ($R = 0$).

TABLE 1

Volume integrals of imaginary potentials compared with phenomenological fits

| Potential E [MeV] | 122 | 160 | 200 | Ref. |
|----------------------|-----|-----|-----|------------------------------|
| microscopic OMP | 182 | 189 | 198 | this work |
| standard parameters | 160 | 176 | 199 | table 1, ref. ¹⁷⁾ |
| +improved spin orbit | 114 | 139 | 139 | table 2, ref. ¹⁷⁾ |
| double Woods-Saxon | 116 | 112 | 128 | table 3, ref. ¹⁷⁾ |

shown in fig. 3. The most severe effect of this correction is to reduce the theoretical total reaction cross section to 225 mb in good agreement with the data. The neglect of this correction produces a reaction cross section which is too high but has virtually no effect on the angular distributions of differential cross sections and polarizations.

In figs. 4 and 5 the real and imaginary spin-orbit potentials are displayed. Their form factors essentially reflect the usual Thomas form $((1/r)\delta\rho/\delta r)$, the density dependence of the spin-orbit interaction modifying this slightly. The approximate energy dependence of the strengths shown as insertions correspond to the strength values at 2 fm. Both potentials decrease in strength with increasing energy. The actual energy dependence shows a flat maximum for the imaginary strength at about 122 MeV decreasing towards higher and lower energies. The reproduction of

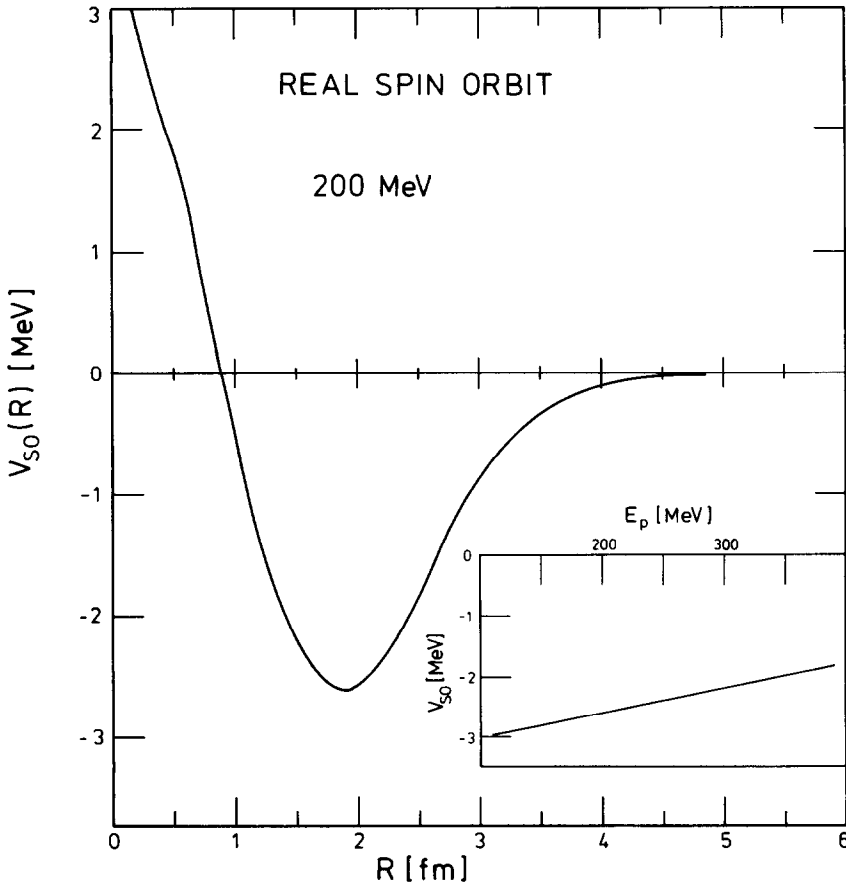


Fig. 4. The microscopic real spin-orbit form factor at 200 MeV. The insert shows the energy variation of the strength at the peak ($R = 2$ fm).

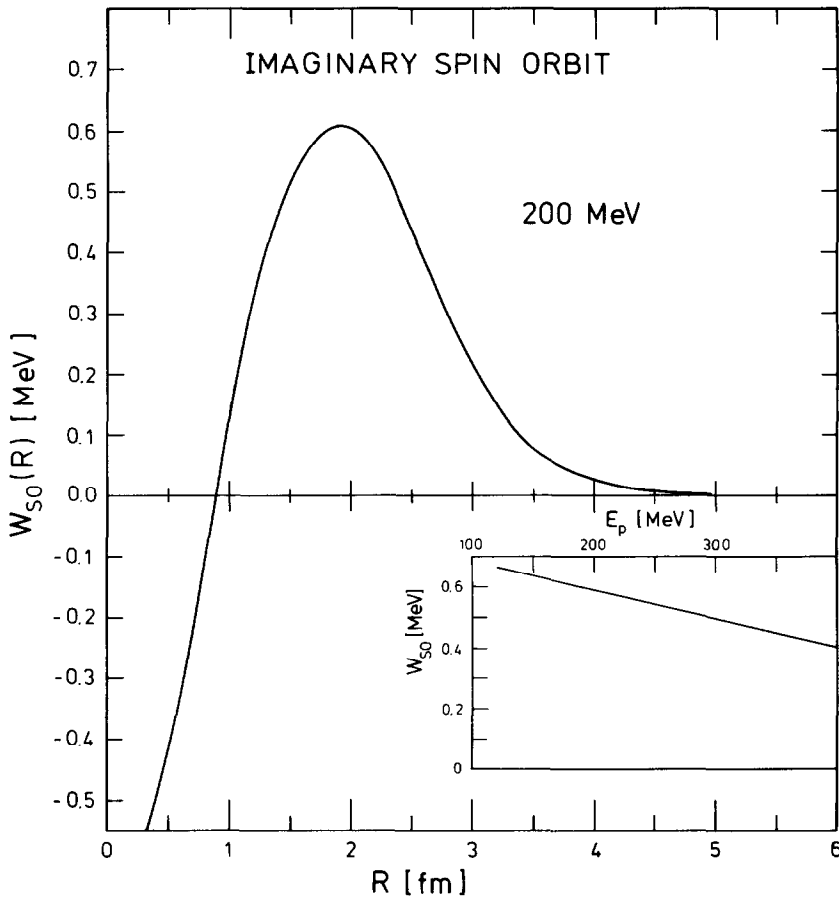


Fig. 5. The microscopic imaginary spin-orbit form factor at 200 MeV. The insert shows the approximate energy variation of the strength at the peak ($R = 2$ fm).

the polarization data with this microscopic optical potential leaves little doubt as to the correctness of the prescription for the spin-orbit potential. The comparison with data can be seen in figs. 6 to 9. The dashed curve in fig. 9 shows the results obtained with an optical model potential derived from the free (i.e. $k_F = 0$ density-independent) t -matrix.

Theoretical predictions between 150 MeV and 400 MeV were computed to stimulate measurements in the hitherto largely ignored energy region between 200 and 400 MeV and are shown in figs. 10 and 11. The challenge for measurements lies in the verification of cross-section and polarization data beyond 1000 MeV/c. Data at 160 MeV and 200 MeV have already indicated strong diffraction effects near 1000 MeV/c which are not reproduced theoretically. With this remark we

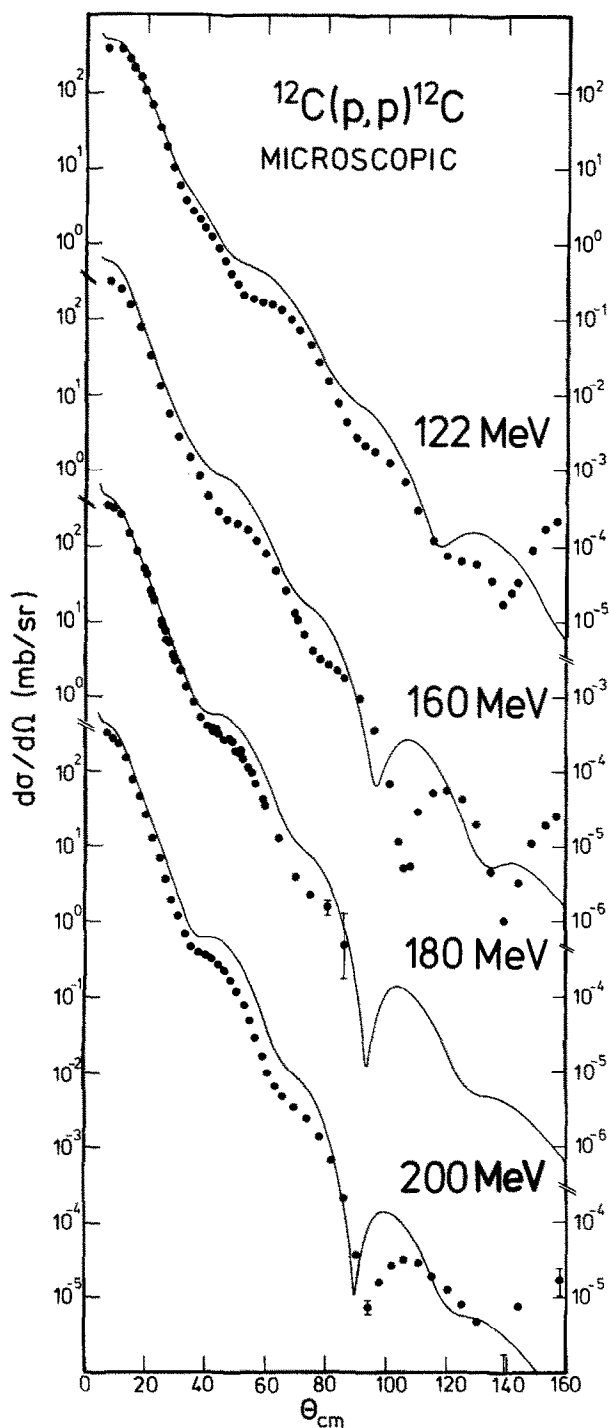


Fig. 6. The angular distribution of the cross sections for elastic scattering calculated using the microscopic optical model based on the density distribution of Meyer *et al.*¹⁷⁾ for incident energies of 122, 160, 180 and 200 MeV compared with the experimental data^{17,18,26)}.

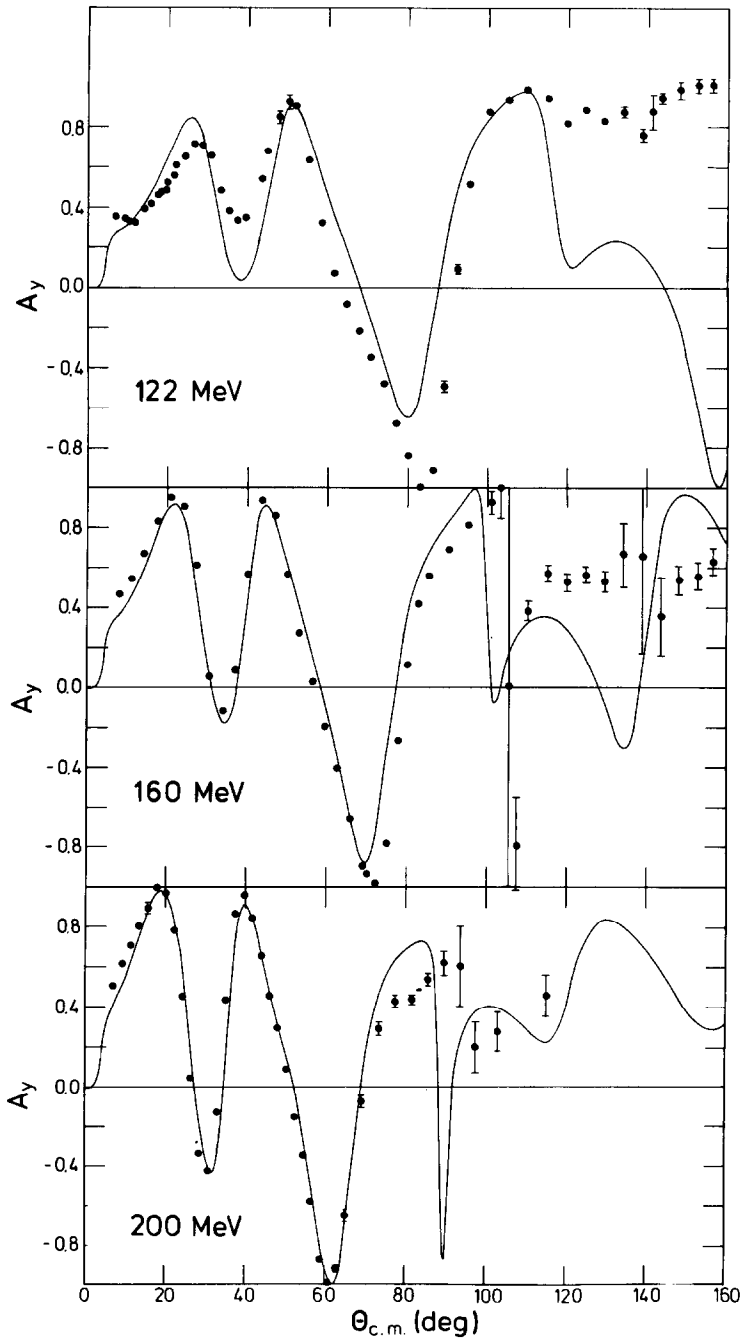


Fig. 7. The angular distributions of the polarization calculated with the microscopic optical potential for 122, 160 and 200 MeV compared with the data ^{17,18}).

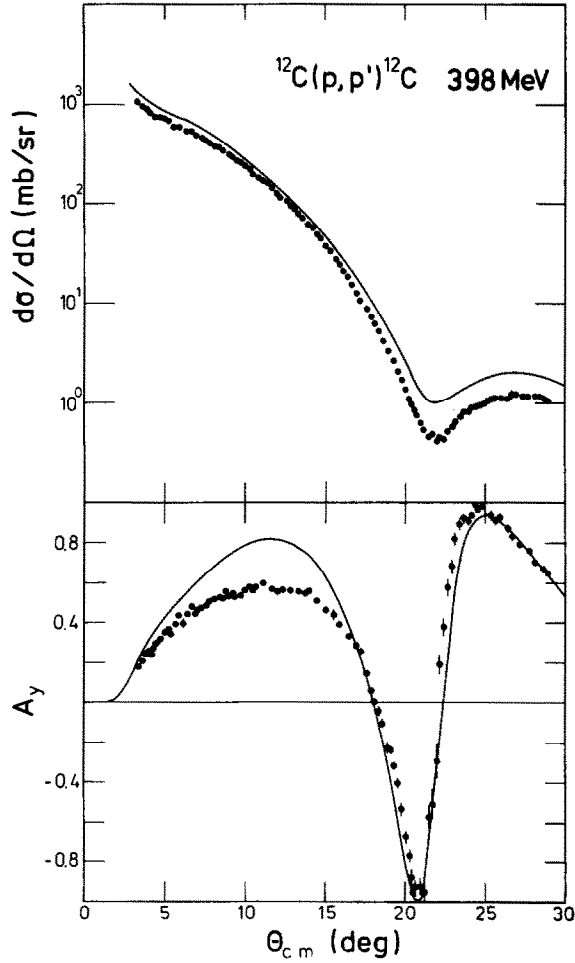


Fig. 8. The angular distributions for elastic scattering at 398 MeV calculated with the microscopic optical potential compared with experimental data ²⁷⁾.

refer to the failure in the analysis shown in fig. 6 for data beyond 130°. At present we attribute this failure mainly to deficiencies in the local equivalent potential as compared to an exact non-local optical model treatment together with improved versions of effective interactions. Coupled-channels test calculations ²⁰⁾ which couple intermediate $\Delta(3,3)$ -hole excitations provide one explanation for this unexpected rise in the differential cross section at backward angles. A complete set of experimental data between 150 and 350 MeV could help to clarify the status of this anomaly and its relationship, if any, to isobaric degrees of freedom.

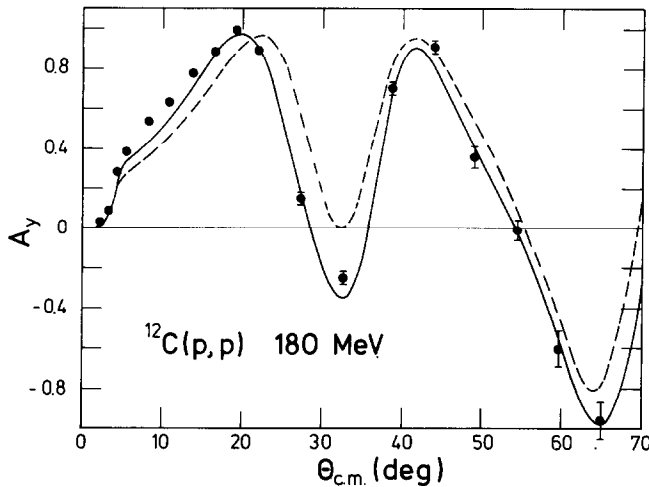


Fig. 9. The polarization calculated from the microscopic optical potential (MOP) at 180 MeV compared with the data. The dashed curve results from a MOP calculated with the density-independent free t -matrix while the full curve corresponds to a MOP based on the fully density-dependent interaction.

4. Inelastic scattering

After studying elastic scattering with the nuclear matter t -matrix approach inelastic studies represent a natural extension. The purpose of these studies may again be considered a test of the effective interaction putting different weight on the individual components as compared to the elastic channel.

Inelastic scattering in ^{12}C is generally done to some prominent states which can be classified as members of the ground-state rotational band, negative-parity states which represent shell-model-like excitations from the p- to sd-shell plus more complicated excitations. Exceptional are excitations within the p-shell which require spin-flip and/or isospin-flip. To the latter category we attribute the non-normal-parity states $J^\pi = 1^+$ at 12.71 MeV and 15.11 MeV. Their isospins are known to be $T = 0$ and $T = 1$, respectively. These two states are strongly excited by inelastic proton scattering and they are considered to be selective to various components of the effective interaction. Particular sensitivity is found in the tensor and spin-orbit components. Normal-parity states have been analysed recently and we therefore concentrate on the above-mentioned non-normal-parity states. These have been of interest in many other studies and we have found experimental data at 5 energies. We have analysed all available data between 120 MeV and 400 MeV, which comprises of differential cross sections, analyzing powers, polarization-analyzing power difference and spin-flip probabilities. The structure information required for these transitions are the spectroscopic amplitudes together with the shell-model basis which is usually chosen to be a harmonic oscillator (optionally a

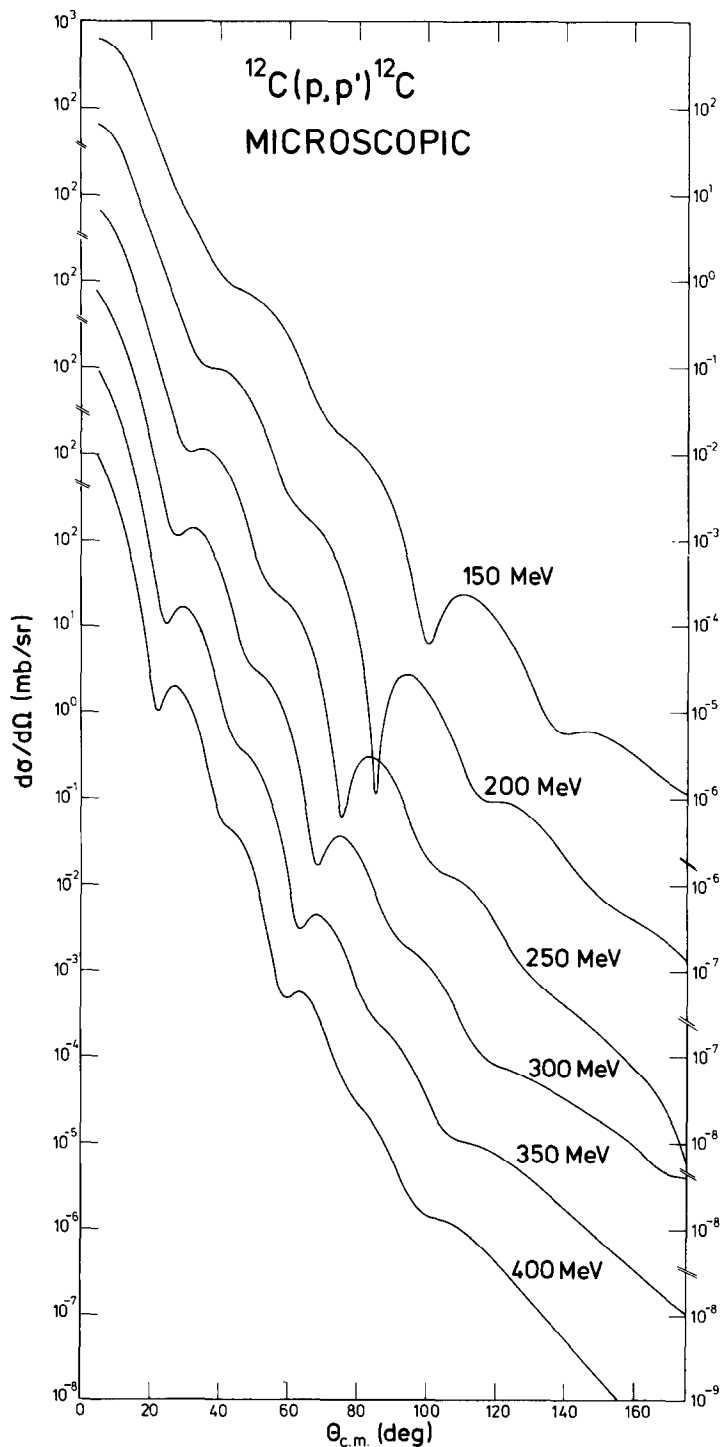


Fig. 10. The energy variation of the proton elastic scattering cross sections between 150 and 400 MeV calculated from the MOP.

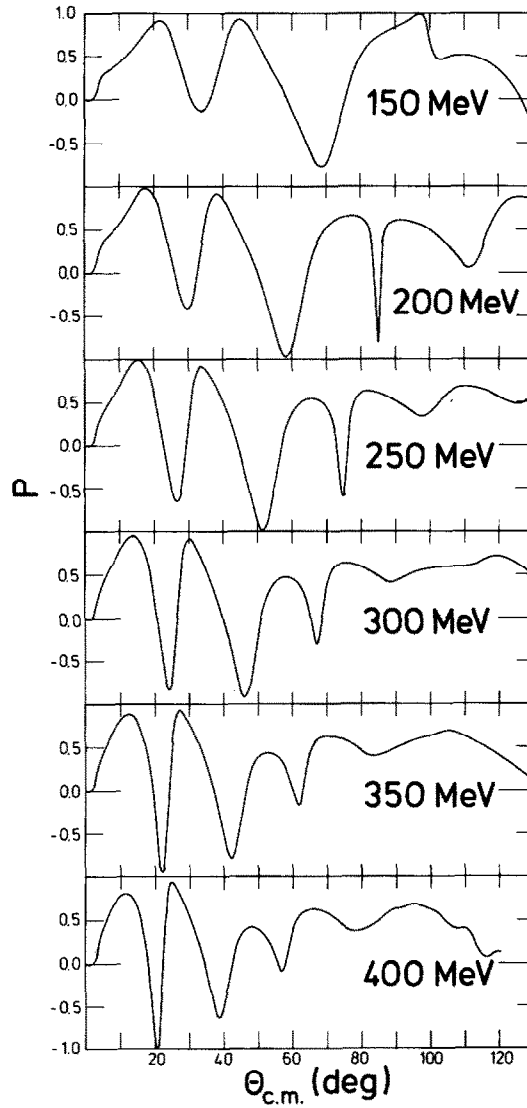


Fig. 11. The polarization corresponding to the calculations shown in fig. 10.

Woods-Saxon basis) which is known to reproduce the best transition rates yet available in a structure calculation and possibly the electron scattering form factors. For the complete inelastic analyses we use the spectroscopy of Cohen and Kurath²³⁾†. In view of several existing experimental data for the 1^+ , $T = 1$ state

† The oscillator parameter was taken for all inelastic calculations as $\alpha = 0.61 \text{ fm}^{-1}$.

and the failure of the Cohen-Kurath structure to reproduce these data²⁴) we should not expect better agreement for the inelastic proton scattering, particularly the higher momentum part. The analyses can more or less only be understood to establish consistency between the microscopic approach to the optical model, using the same t -matrix as transition operator and the application of the antisymmetrised DWBA model in the right energy range. It should help to outline possible failures of the ingredients in a DWIA with its final goal of a completely microscopic analysis of inelastic proton scattering.

The inelastic transition is analysed using the fully antisymmetrised DWTA where the exchange amplitudes are treated exactly with the t -matrix as driving transition operator. We distinguish the DWIA from the DWTA by the sole use of the free t -matrix in the former whilst the latter is based on the density-dependent t -matrix:

$$T_{\text{DWTA}} = \sum_{j_1 j_2} S_{j_1 j_2}^{I, T} \langle \chi_i^{(-)}(\mathbf{r}_0) \phi_{j_2}(\mathbf{r}_1) | t(|\mathbf{r}_0 - \mathbf{r}_1|; \text{LDA}) \times | \{ \chi_i^{(+)}(\mathbf{r}_0) \phi_{j_1}(\mathbf{r}_1) - \chi_i^{(+)}(\mathbf{r}_1) \phi_{j_1}(\mathbf{r}_0) \} \rangle, \quad (36)$$

wherein $S_{j_1 j_2}^{I, T}$ is the spectroscopic factor³²). The notation for the transition operator emphasizes the density dependence and the use of the LDA. Similar to the elastic case, $t(|\mathbf{r}_0 - \mathbf{r}_1|; \text{LDA})$ in eq. (36) requires a recipe for handling the dependence on the two coordinates \mathbf{r}_0 and \mathbf{r}_1 which point into different density regions. We have chosen the geometric mean,

$$t(|\mathbf{r}_0 - \mathbf{r}_1|; \text{LDA}) = \{ t(|\mathbf{r}_0 - \mathbf{r}_1|, k_F(\mathbf{r}_0)) t(|\mathbf{r}_0 - \mathbf{r}_1|, k_F(\mathbf{r}_1)) \}^{\frac{1}{2}}, \quad (37a)$$

and alternatively the arithmetic mean,

$$t(|\mathbf{r}_0 - \mathbf{r}_1|; \text{LDA}) = \frac{1}{2} \{ t(|\mathbf{r}_0 - \mathbf{r}_1|, k_F(\mathbf{r}_0)) + t(|\mathbf{r}_0 - \mathbf{r}_1|, k_F(\mathbf{r}_1)) \}. \quad (37b)$$

In practice these two prescriptions are not distinguishable. For the computations we have used the program DWBA 82 [ref.³³] which is a modified version of Raynal's most recently developed DWBA 79. This program contains the same formalism as used in DWBA 70 but is now equivalent in programming structure to ECIS [ref.³⁴]. It facilitates computations including all the complications of exchange and density dependence up to 1 GeV with sufficient numerical accuracy. There are no limitations in the use of phenomenological or microscopic optical potentials or in the number of partial waves and multipoles. The relevant tensor algebra remains unchanged and can be found in the literature.

We distinguish in our analyses inelastic transitions in which the distorted waves $\chi^{(\pm)}$ are computed with phenomenological optical potentials with parameters taken from the literature and cases where the distorted waves are calculated from the microscopic optical models which were discussed in the previous section. The first

type of calculation uses not only standard Woods-Saxon potentials but also the recently proposed DWS parametrization combined with a modified spin-orbit potential. We take the relevant parameters from ref. ¹⁷). The 155 MeV analysis uses interpolated parameters based on table 3 of this reference.

The differential cross sections for the isoscalar transition using the phenomenological potentials for all energies shown in fig. 12 significantly overestimate the low momentum transfer region and underestimate the high momentum region. The analysing power predictions shown in fig. 13 are in qualitative agreement with the data. The situation at 398 MeV, presented in fig. 14 confirms these features from the lower-energy régime with a somewhat less drastic difference between experiment and theory.

In fig. 15 are displayed the fully microscopic calculations which differ from the previous results in the use of the microscopic optical potentials as generators of the distorted waves instead of the phenomenological potentials. The spectroscopic information and effective interaction for the transition were the same. We observe a drastic improvement but still lack the required cross-section reduction for low

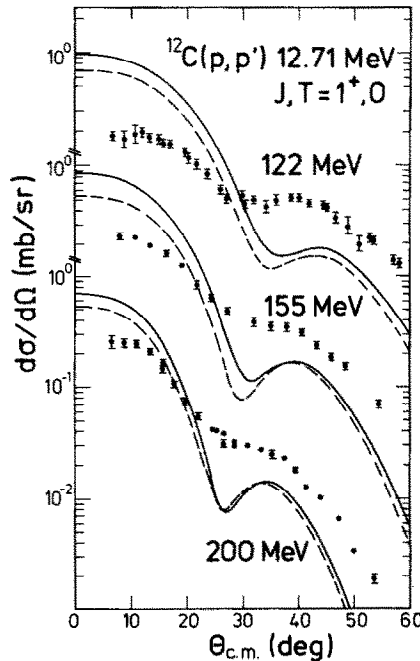


Fig. 12. The differential cross sections for the $J = 1^+$, $T = 0$ (12.71 MeV) transition in $^{12}\text{C}(p, p')$ calculated using phenomenological optical potentials. The dashed curves are calculated with standard Woods-Saxon (SWS) form factors and the full lines with double Woods-Saxon (DWS) and modified spin-orbit (MSO) form factors. The oscillator parameter was chosen as $\alpha = 0.61 \text{ fm}^{-1}$ for all the inelastic studies reported herein.

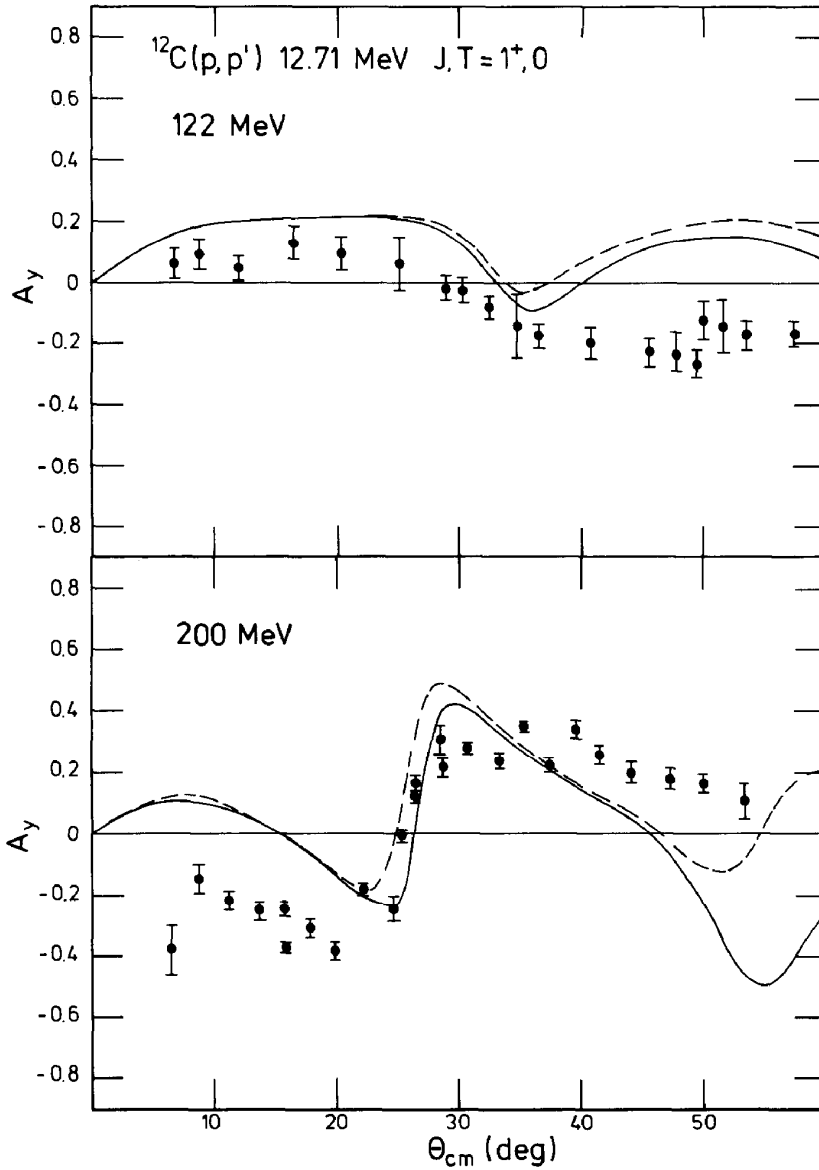


Fig. 13. The analysing powers for the isoscalar transition. See fig. 12 caption for details.

momentum transfers. All the microscopic calculations reported herein (except those at 398 MeV) involve no renormalization. This is important since the predictions shown in fig. 15 could be brought into good agreement with the data above 250 MeV/c by a renormalization of the theoretical curves by a factor of 2. We are

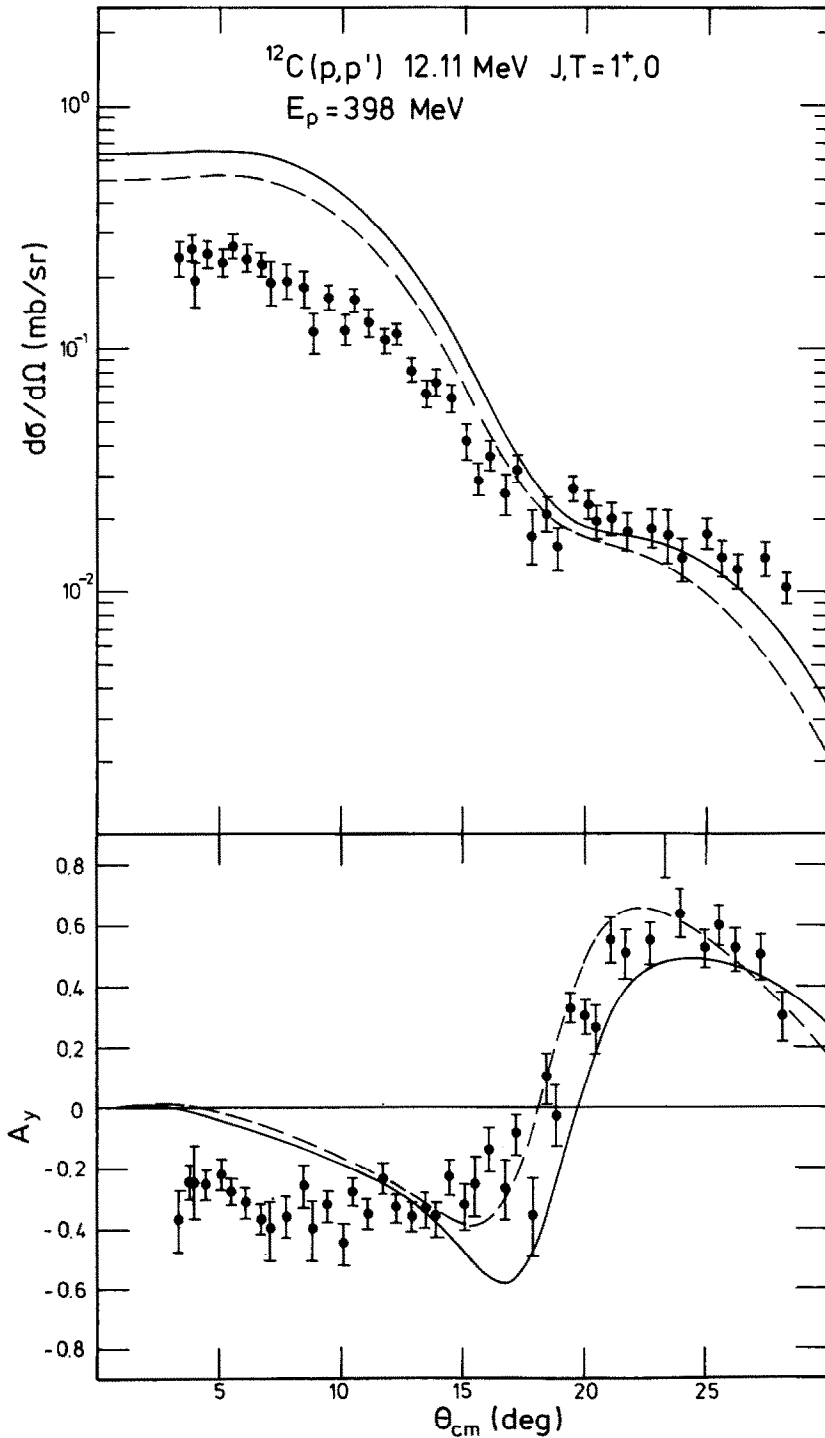


Fig. 14. The angular distributions for the isoscalar transition for an incident energy of 398 MeV calculated using phenomenological potentials compared with the experimental data. Both the dashed ²⁷⁾ and continuous curves ³⁵⁾ were calculated with standard shape form factors.

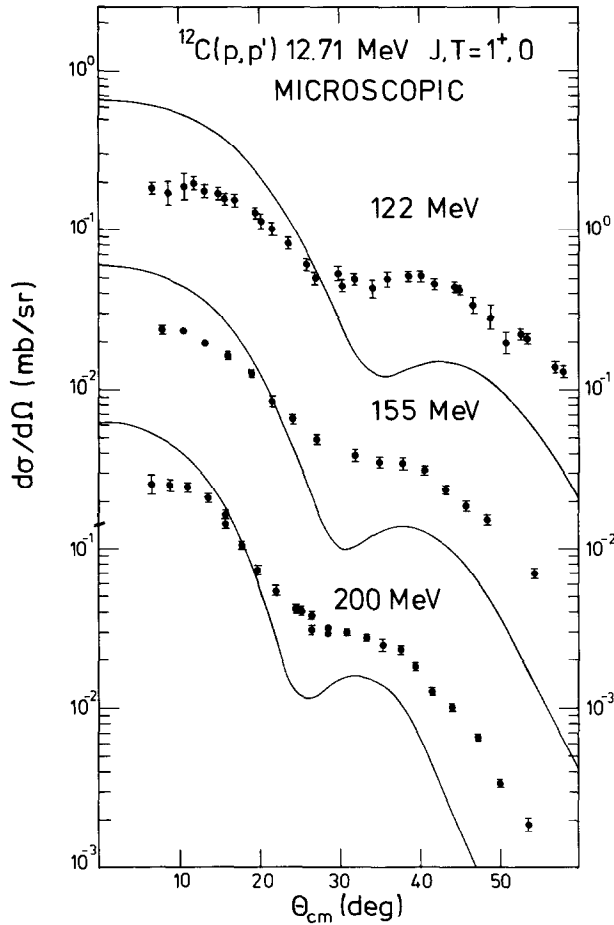


Fig. 15. The differential cross sections for the isoscalar transition calculated fully microscopically (i.e. using microscopic optical potentials and the density-dependent t -matrix as transition operator) and compared with experiment. This figure should be compared with fig. 12. Note that these results do not include any renormalization.

tempted to claim, however, that such agreement is fortuitous and that the discrepancy between theory and experiment for this isoscalar transition is due to the lack of a satisfactory description of the transition density as proposed by the Cohen-Kurath wave functions, a feature which is already known from electron scattering experiments. The behaviour in this instance suggests that large shell-breaking²⁴⁾ effects cause significant contributions of at least $2\hbar\omega$ excitation. Such extended shell-model wave functions feasibly contain the long-range modification producing the reduced low momentum transfer components and short-range modifications yielding enhanced high-momentum transfer components. Proposed

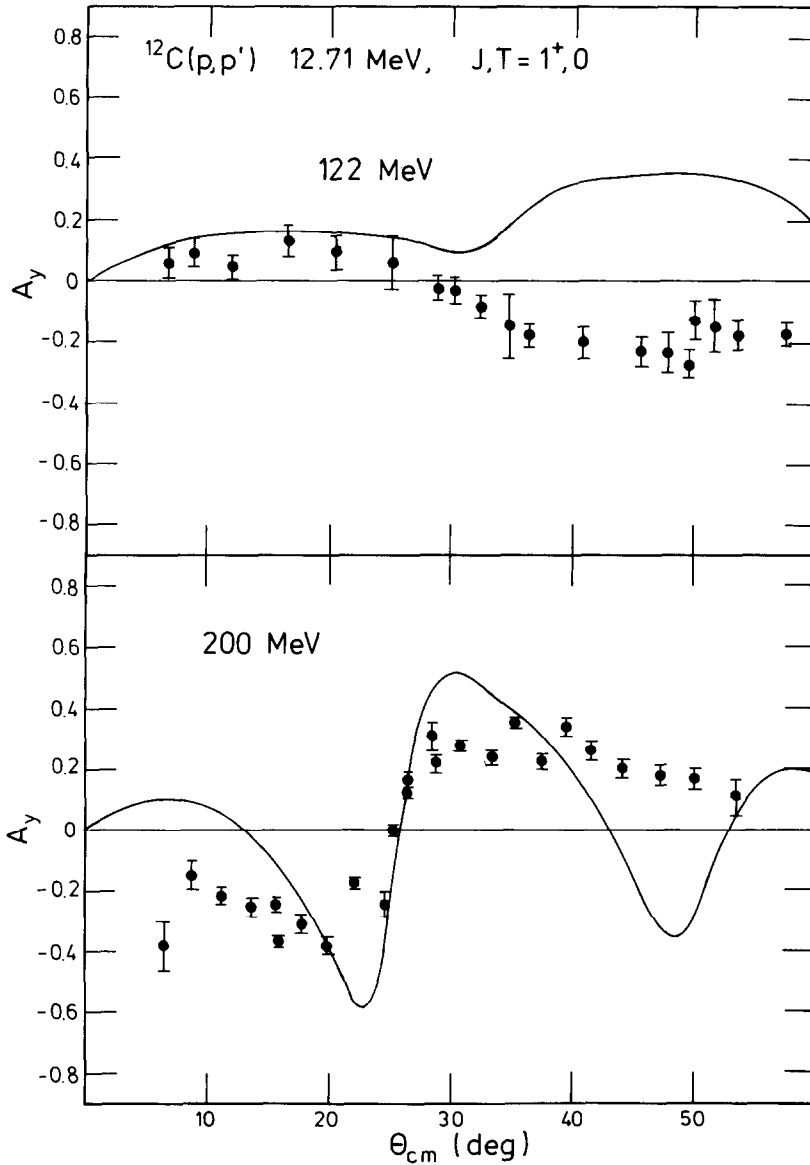


Fig. 16. The analysing powers obtained from the fully microscopic calculations. To be compared with fig. 13.

reasonable isospin breaking²⁴) is insufficient as far as a calculation restricted to the 1p shell is concerned. The analysing power data fits (fig. 16) confirm the so-far discussed features of the isoscalar transition and we see improvement occurring for the pure microscopic calculation as compared to the phenomenological case. The

fact that no renormalization is required as well as the qualitative agreement gives confidence in the usefulness of the effective interaction. The 398 MeV data are again better reproduced in the full microscopic calculation, fig. 17.

For the case of the isovector transition the calculations of the differential cross sections using the phenomenological optical potentials at the lower energies are shown in figs. 18 and 19. This transition has been extensively studied using (e, e')

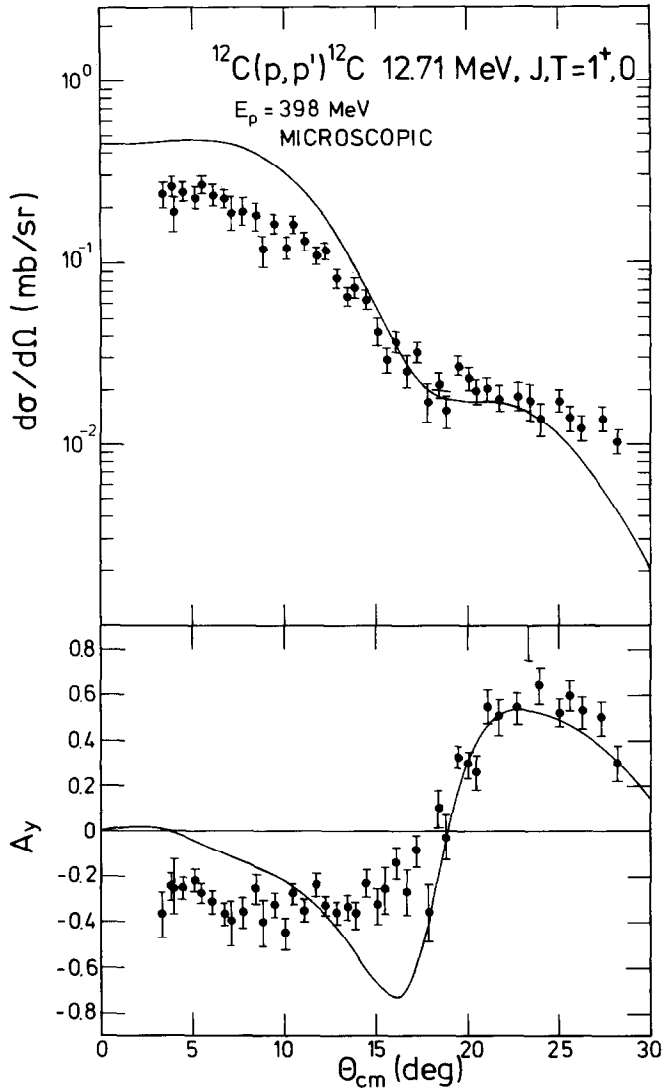


Fig. 17. The angular distributions resulting from the fully microscopic calculations for 398 MeV protons. To be compared with fig. 14.

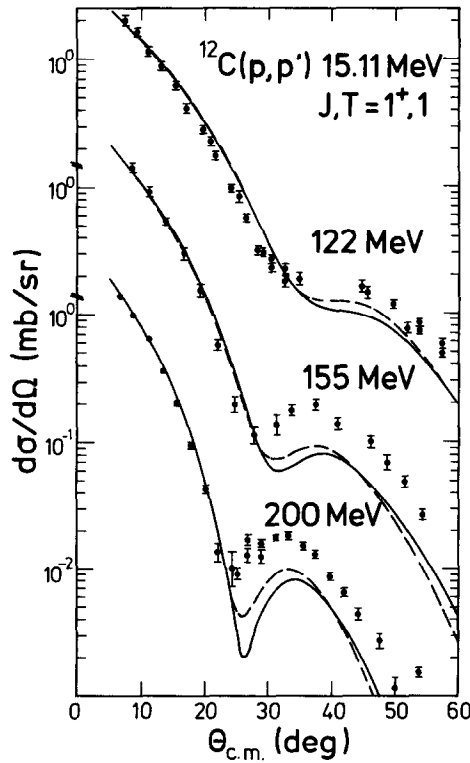


Fig. 18. The differential cross sections for the $J = 1^+$, $T = 1$ (15.11 MeV) transition in $^{12}\text{C}(p,p')$ calculated using phenomenological optical potentials. The dashed curves correspond to SWS calculations and have been renormalized by 0.9 (122 MeV) and 0.8 (155 MeV and 200 MeV). The full curves used the DWS+MSO form factors and were renormalized by 0.7 (122 MeV) and 0.6 (155 and 200 MeV).

and (p,p') reactions. The former ²⁴⁾ have shown the inadequacy of the Cohen-Kurath wave functions in explaining the magnetic form factor, particularly at momentum transfers above 220 MeV/c. Indeed subsequent investigation has produced modified p-shell wave functions which explain the (e,e') data to a much better degree ²⁴⁾. However, the use of this modified spectroscopy in (p,p') calculations has been shown ¹⁾ to produce results essentially identical to those using pure Cohen-Kurath wave functions since the transition operator involved is sensitive only to the features of the structure that are basically similar in both models. As we are of the opinion that the major discrepancies are due to the lack of higher $\hbar\omega$ excitations anyway and to keep consistency with the results discussed above for the isoscalar transition (for which these modified transition densities are not available), we have again used only the Cohen-Kurath wave functions.

The phenomenological optical potentials used for the 398 MeV calculations are

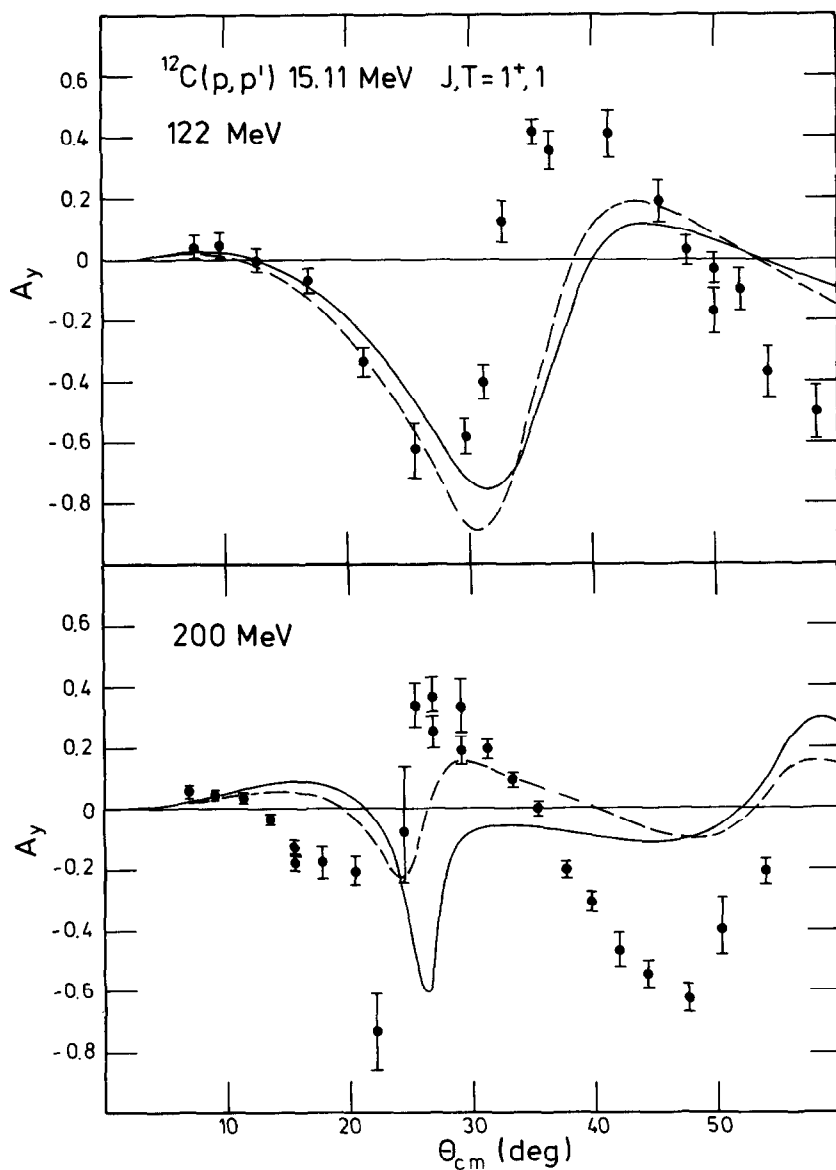


Fig. 19. The analysing powers corresponding to the calculations of fig. 18.

given in table 2 and the resulting differential cross sections and analysing powers shown in fig. 20. Of particular interest is the comparison of the analysing power with the data. This displays a high sensitivity to the sign of the imaginary spin-orbit potential. The Cupid 27) potential has in this component the opposite sign to

TABLE 2
Phenomenological optical model parameters for $E_p = 398$ MeV

| V_0 | r_0 | a_0 | W | r_W | a_W | V_{LS} | r_{VLS} | a_{VLS} | W_{LS} | r_{WLS} | a_{WLS} | r_C | Ref. |
|--------|-------|--------|---------|-------|--------|----------|-----------|-----------|----------|-----------|-----------|-------|----------------------|
| -3.226 | 1.084 | 0.591 | 20.939 | 1.129 | 0.629 | 3.177 | 0.933 | 0.611 | -2.793 | 0.999 | 0.530 | 1.05 | HAM ³⁵⁾ |
| 26.239 | 1.249 | 0.4741 | 25.9308 | 1.077 | 0.5935 | 1.9692 | 0.9945 | 0.4962 | 2.822 | 0.9705 | 0.5071 | 1.05 | CUPID ²⁷⁾ |

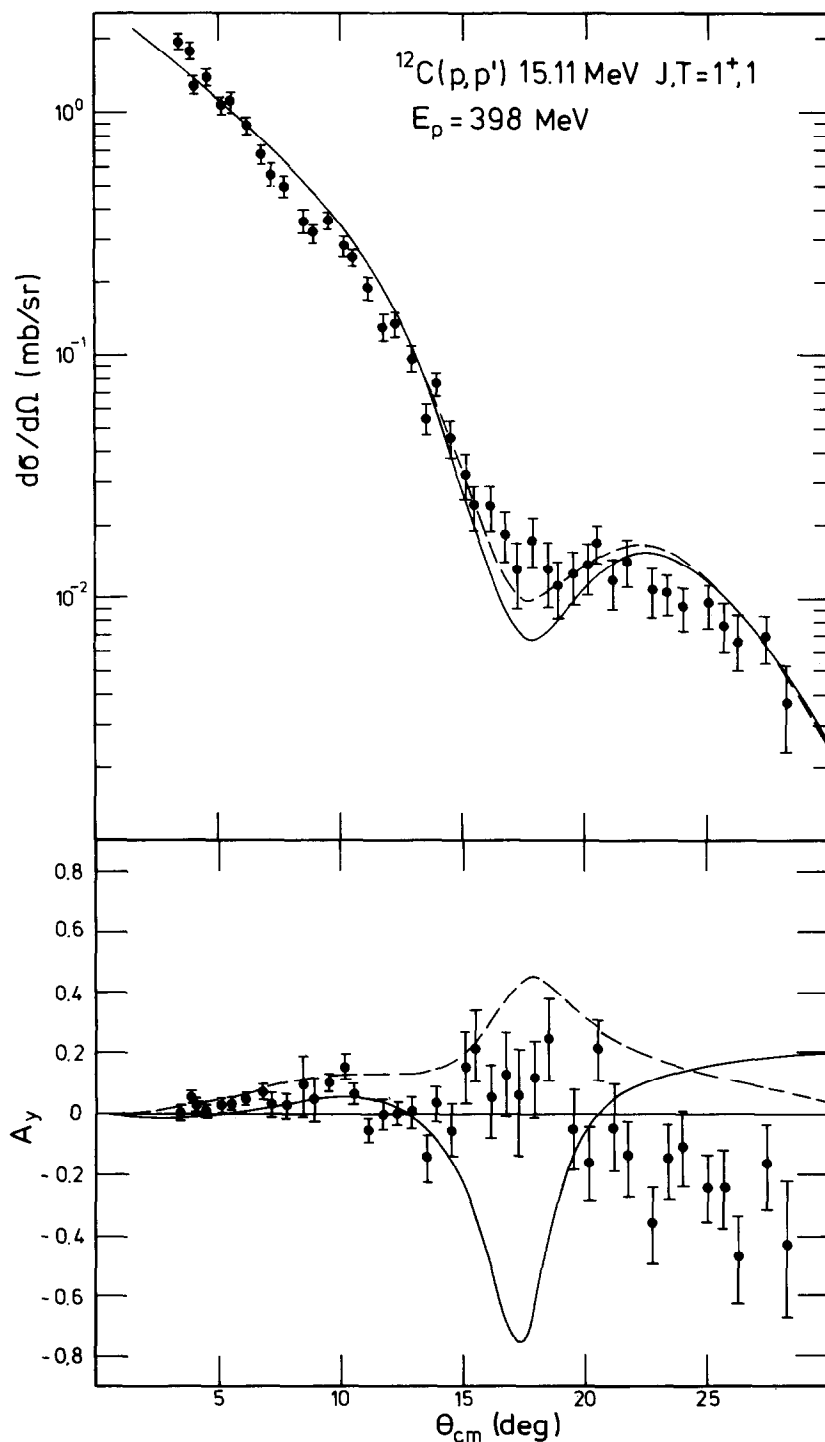


Fig. 20. The angular distributions for the isovector transition for 398 MeV incident protons calculated with two different phenomenological potentials. The full curve is the Hamburg potential³⁵⁾ of table 2 while the dashed curve corresponds to the CUPID potential²⁷⁾.

the microscopic and phenomenological potentials. This ambiguity in sign yields little change for the isoscalar transition where the general structure is quite well reproduced but it allows for drastic variations to occur in the isovector transition. Only the Cupid potential of table 2 results in a favourable reproduction of the data whereas the microscopic calculations shown in fig. 21 as well as other phenomenological potentials contradict experiment. To resolve this problem it has

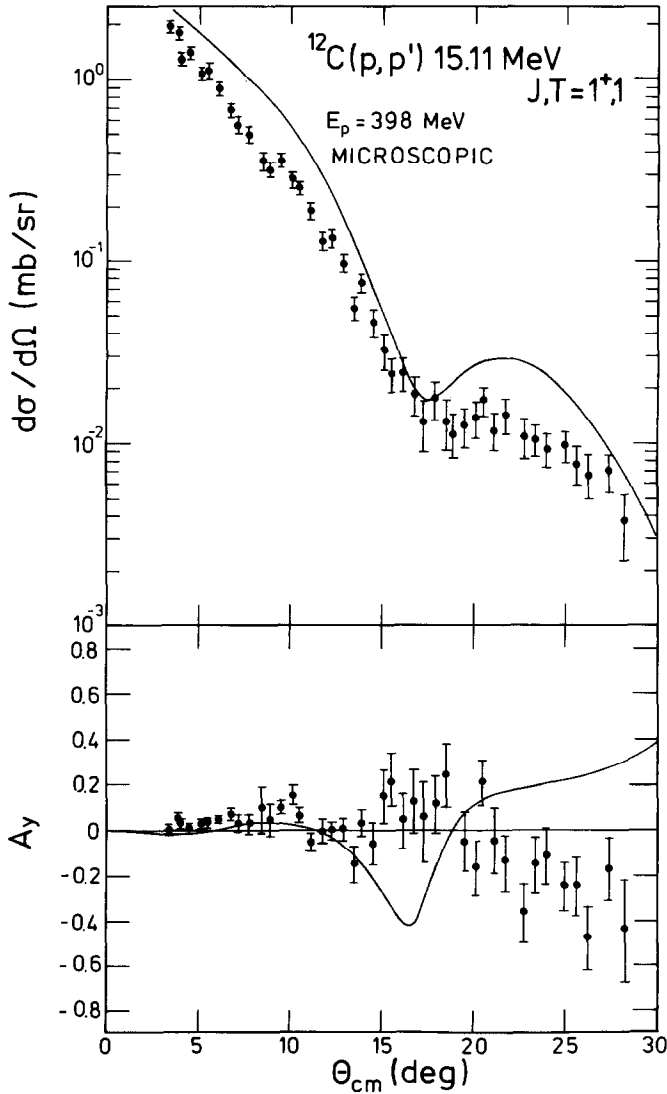


Fig. 21. The angular distributions for the isovector transition for 398 MeV incident protons calculated fully microscopically. The curve has not been renormalized.

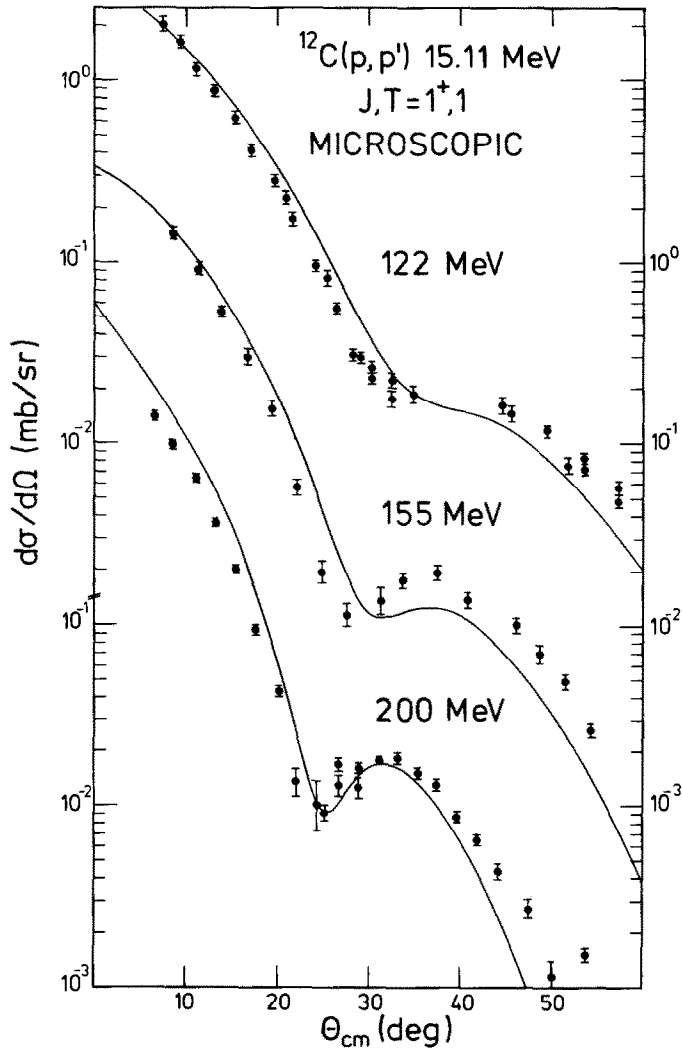


Fig. 22. The differential cross sections for the isovector transition calculated fully microscopically. These curves include no renormalization. They should be compared with the phenomenological curves of fig. 18.

been suggested that the experimental data for the isovector transition should have opposite sign. There is no solution known which resolves this problem, particularly as we have more confidence in the $T = 1$ form factor than for the $T = 0$ transition. Perhaps the study of an isovector dipole transition in other nuclei where ambiguities in the wave function are less severe would shed light on this question.

As a final comparison with experimental data we show in figs. 22 and 23 the fully

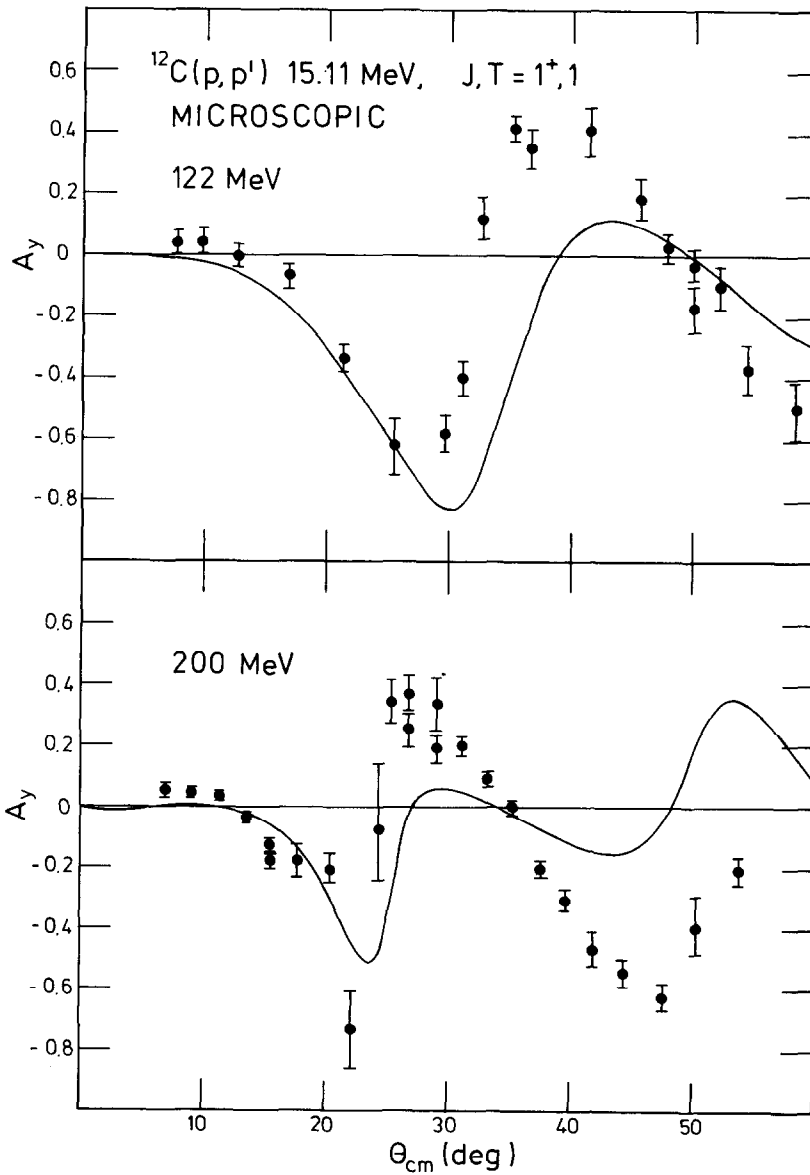


Fig. 23. The analysing powers for the isovector transition calculated fully microscopically. They should be compared with those in fig. 19.

microscopic predictions for the angular distributions. The polarization analysing power difference at 150 MeV and the spin-flip probability at 397 MeV are shown in figs. 24 and 25, respectively. The former merely reinforces our conclusions concerning

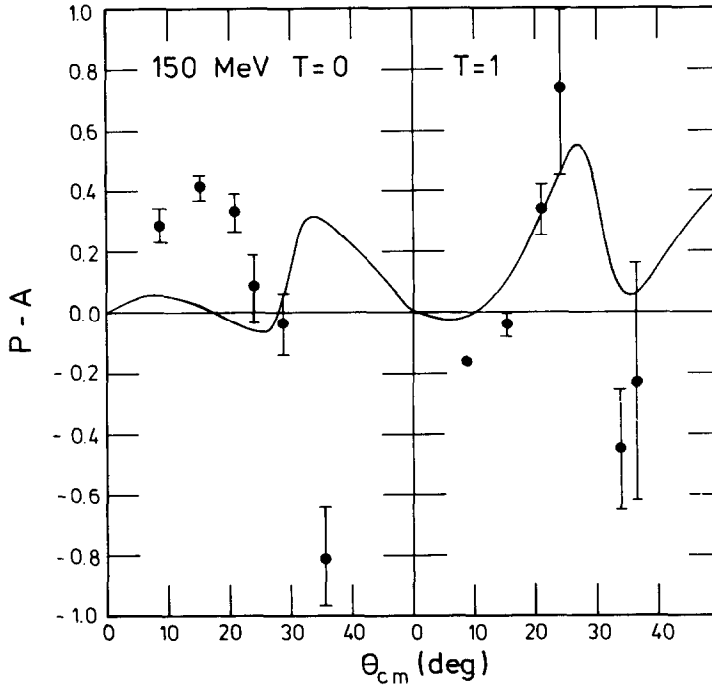


Fig. 24. Polarization minus analysing power for both the isovector and isoscalar transitions calculated fully microscopically compared to the data ³⁷⁾ at 150 MeV.

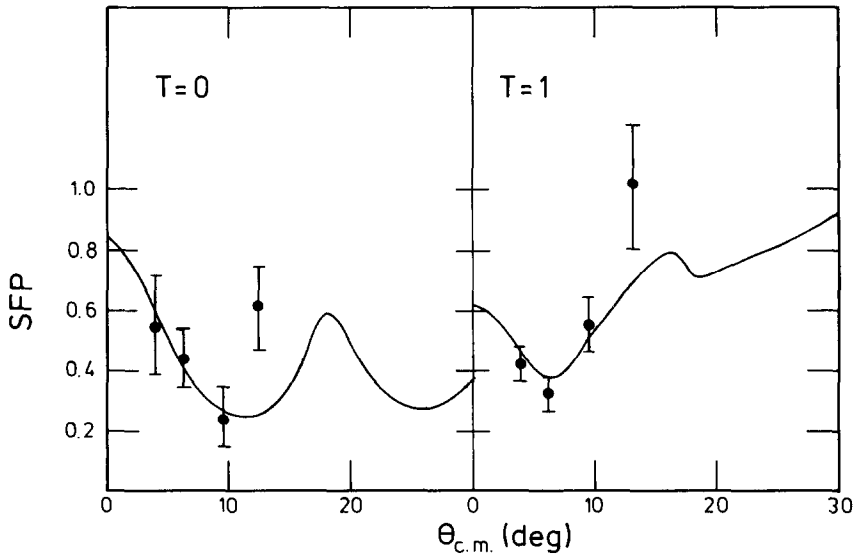


Fig. 25. Spin-flip probability for both transitions calculated fully microscopically and compared with the data at 397 MeV [ref. ³⁸⁾].

the problems with the isoscalar form factor at all momentum transfers and the isovector form factor at higher momentum transfers. The latter indicates that spin-flip probabilities are not sensitive to the deficiencies in either form factor, at least for lower momentum transfers.

The two transitions described above sample different linear combinations of the components of the effective interaction due to their differing isospin nature. The $T = 0$ transition is primarily sensitive to the V_σ component, expressed in terms of relative spin-isospin states in the form of

$$V_\sigma = \frac{1}{8}(-3t^{\text{SE}} + t^{\text{TE}} - t^{\text{SO}} + 3t^{\text{TO}}). \quad (38)$$

The $T^- = 1$ transition requires in addition to a spin-flip, an isospin-flip and therefore selects out $V_{\sigma\tau}$ which is a linear combination of the spin-isospin channels:

$$V_{\sigma\tau} = \frac{1}{8}(-t^{\text{SE}} - t^{\text{TE}} + t^{\text{SO}} + t^{\text{TO}}). \quad (39)$$

The isoscalar and isovector non-central force components are linear combinations of the $T = 0$ and $T = 1$ components, respectively. In detail, these are given by

$$V_{LS} = \frac{1}{4}(t^{\text{LSE}} + 3t^{\text{LSO}}), \quad (40)$$

$$V_{LS\tau} = \frac{1}{4}(-t^{\text{LSE}} + t^{\text{LSO}}), \quad (41)$$

$$V_{\text{T}} = \frac{1}{4}(t^{\text{TNE}} + 3t^{\text{TNO}}), \quad (42)$$

$$V_{\text{T}\tau} = \frac{1}{4}(-t^{\text{TNE}} + t^{\text{TNO}}). \quad (43)$$

Considering the relative signs of the various force components it is a quite natural result that the isoscalar transitions are dominated in the non-central components by the spin-orbit force whereas the isovector transitions are dominated by the tensor force. This can be seen in figs. 26 and 27. Quantitatively, this dominance is energy dependent but grossly speaking it is valid throughout the energy region investigated herein.

Lower-energy data have been analysed in order to investigate the differences between the isovector and isoscalar transition with the aim of ascertaining the reaction mechanism and the effective interactions³⁶). It was found that two-step reaction processes via formation of an intermediate deuteron are of little importance as compared to contributions from the spin-orbit and tensor interactions. This result remains valid for high energies where we also confirm that the structural differences of these two transitions rests on the interaction and to a large degree on the nuclear structure wave functions. It is our opinion that the low-energy analysis should be insensitive with regard to the detailed description of the

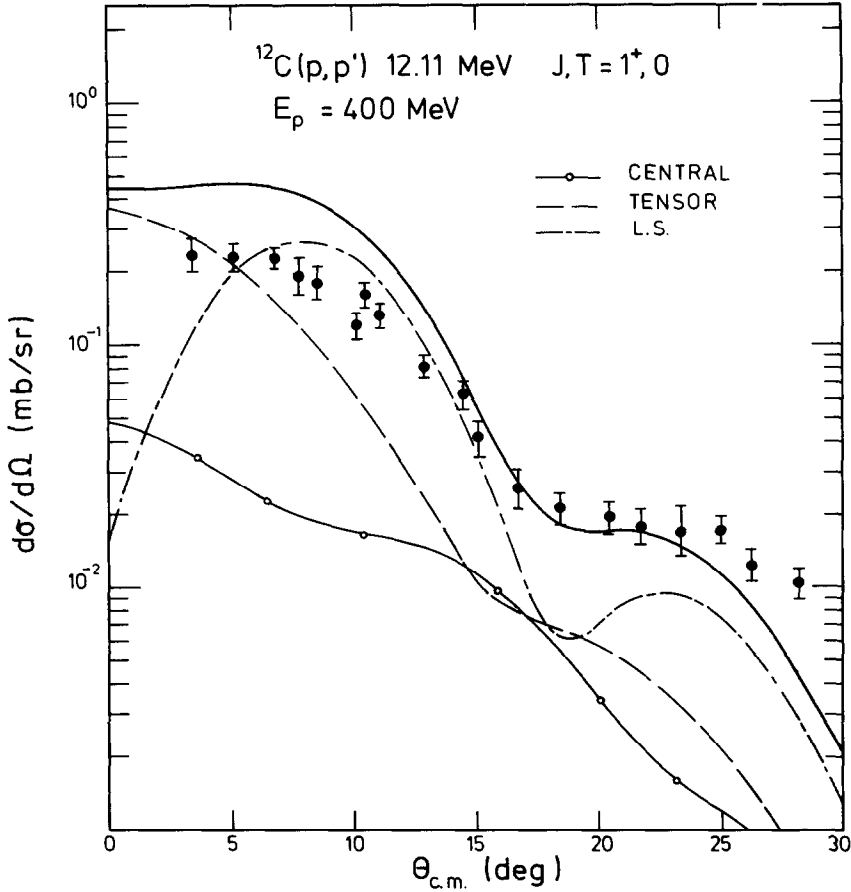


Fig. 26. The differential cross section for the isoscalar transition for 400 MeV protons (full curve) showing the contributions from the central (bubbled curve) tensor (dashed curve) and spin-orbit (long-short dashed curve) transition operators.

transition densities since they are only sensitive to the momentum transfer region from 0 to 1.5 fm^{-1} . As comparisons with electron scattering show form-factor difficulties arise for momentum transfers beyond these limits.

5. Conclusion

This paper demonstrates the excellent quality of the theoretical fits to experimental scattering data that are possible with consistent parameter-free calculations for both elastic and inelastic proton scattering at intermediate energies. In addition, it has provided a useful critique of the underlying theory and indicated

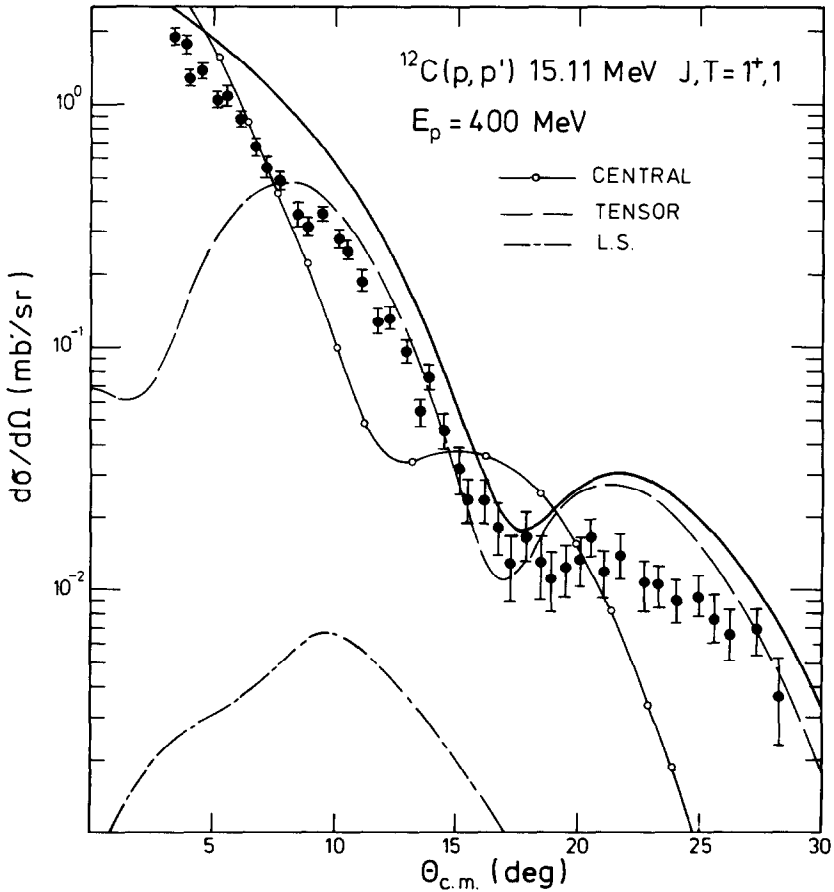


Fig. 27. The differential cross section for the isovector transition for 400 MeV protons. See fig. 26 for details.

the areas where the approximations should be refined. We feel confident from the results of this case study that the approximations inherent in the derivation of the effective interaction are now of lesser importance for the final predictions than those in the folded optical potential and the scattering calculations themselves. Thus, before steps are taken to improve on the nuclear matter t -matrix, the non-locality produced by the exchange in the optical model should be treated exactly. Of equal importance at energies above 200 MeV is the question of the actual role played by relativistic effects and the best way to approximate them in scattering calculations involving microscopic optical potentials. Although the nuclear matter t -matrix is obtained from a non-relativistic many-body theory framework, it is based on an interaction that has been fitted to NN scattering data for energies up to 330 MeV [ref. ¹⁶], and which inherently includes, therefore, some degree of

relativistic correction. Hence, as can be seen from the 400 MeV calculations included herein, the standard semi-relativistic approximation which is often used for phenomenological optical potential calculations overcorrects in the microscopic optical potential case.

Apart from the above-mentioned points it should be remembered that a fully microscopic parameter-free calculation can only be as good as the least well-known input will allow. For elastic scattering this is illustrated by the breakdown of the theory when extrapolated to momentum transfers above the limit to which the form factor is known accurately from electron scattering studies. In the inelastic case the failure to reproduce the isoscalar transition data argues strongly the need for better spectroscopic amplitudes, as does the breakdown in the isovector transitions for higher momentum transfers.

It is worthwhile to note in passing that problems associated with the high momentum transfer region will make it extremely difficult to isolate the effects due to mesonic degrees of freedom. In particular, the isovector transition in carbon has been regarded as a strong candidate for the observation of precritical phenomena^{3,21)} and quenching effects of the Gamow-Teller transition have been predicted. However, as can be seen from results presented herein, the microscopic and two phenomenological optical potentials provide distorted waves which can give substantially different predictions at backward angles where precursor effects are predicted. Although this problem can be circumvented by the use of fully microscopic optical models based on sufficiently accurately known density distributions there are still other problems such as the lack of good spectroscopy and a question of the need for higher-order terms to be contended with.

As a summary it has been shown that the microscopic optical model can give predictions for elastic scattering data that is in some cases better than many phenomenological potentials, particularly for polarization phenomena. The use of ^{12}C as a case study of inelastic scattering is somewhat weakened by the poor spectroscopy available, but even so provides an interesting comparison of the predictions of microscopic parameter-free analyses and those based on good phenomenological potentials. In the absence of an exact completely microscopic relativistic theory it is heartening to note the large degree of success that can be obtained from first-principle non-relativistic calculations. This indicates that such calculations will provide a useful and necessary means in intermediate-energy nucleon-nucleus analyses for some time to come.

References

- 1) W. G. Love, in Proc. LAMPF Workshop on nuclear structure studies with intermediate energy probes, Los Alamos, 1980;
H. J. Weber, *F. Phys.* **24**, (1976) 1
- 2) R. M. DeVries and J. C. Peng, *Phys. Rev. C* **22** (1980) 1055

- 3) J. Delorme, A. Figureau and N. Giraud, *Phys. Lett.* **91B** (1980) 328;
J. Delorme, M. Ericson, A. Figureau and N. Giraud, *Phys. Lett.* **89B** (1980) 327
- 4) C. Gaarde, *Nucl. Phys.* **A396** (1983) 127c;
C. Goodman, *Nucl. Phys.* **A374** (1982) 241c
- 5) S. J. Wallace, *Advances in nuclear physics* vol. **12**, ed. J. W. Negele and E. Vogt (Plenum, NY)
- 6) A. K. Kerman, H. McManus and R. M. Thaler, *Ann. of Phys.* **8** (1959) 551
- 7) L. Ray, *Phys. Rev.* **C19** (1979) 1855;
D. A. Hutcheon, J. M. Cameron, R. P. Liljestrand, P. Kitching, C. A. Miller, W. J. McDonald, D. M. Sheppard, W. C. Olson, G. C. Neilson, H. S. Sherif, D. K. McDaniels, J. R. Tinsley, L. W. Swenson, P. Schwandt, C. E. Stronach and L. Ray, *Phys. Rev. Lett.* **47** (1981) 315
- 8) L. Ray, *Phys. Rev.* **C20** (1979) 1857
- 9) G. W. Hoffmann, L. Ray, M. L. Bartlett, R. Fergeson, J. McGill, E. C. Milner, K. K. Seth, D. Barlow, M. Bosko, S. Iverson, M. Kaletka, A. Saha and D. Smith, *Phys. Rev. Lett.* **47** (1981) 1436
- 10) F. A. Brieva and J. R. Rook, *Nucl. Phys.* **A291** (1977) 219, 317
- 11) J. Hüfner and C. Mahaux, *Ann. of Phys.* **73** (1972) 525
- 12) J. P. Jeukenne, A. Lejeune and C. Mahaux, *Phys. Rev.* **C25** (1976) 83
- 13) Effective interactions in nuclear models and nuclear forces, *Prog. Theor. Phys. Suppl.* **65** (1979)
- 14) H. V. von Geramb, L. Rikus and K. Nakano, in *Proc. RNCP Int. Symp. on light ion reaction mechanism*, 1983, Osaka, Japan, to be published
- 15) C. M. Shakin, in *The interaction between medium energy nucleons in nuclei 1982*, ed. H. O. Meyer (AIP, 1983)
- 16) M. Lacombe, B. Loiseau, J. M. Richard, R. Vinh Mau, J. Côté, P. Pirès and R. de Tourreil, *Phys. Rev.* **C21** (1980) 861
- 17) H. O. Meyer, P. Schwandt, W. W. Jacobs and J. R. Hall, *Phys. Rev.* **C27** (1983) 459;
H. O. Meyer, P. Schwandt, G. L. Moake and P. P. Singh, *Phys. Rev.* **C23** (1981) 616
- 18) J. R. Comfort, G. L. Moake, C. C. Foster, P. Schwandt and W. G. Love, *Phys. Rev.* **C26** (1982) 1800;
J. R. Comfort, G. L. Moake, C. C. Foster, P. Schwandt, C. D. Goodman, J. Rapaport and W. G. Love, *Phys. Rev.* **C24** (1981) 1834, 1844;
J. R. Comfort, R. E. Segel, G. L. Moake, D. W. Miller and W. G. Love, *Phys. Rev.* **C23** (1981) 1858;
J. R. Comfort, S. M. Austin, P. T. Debevec, G. L. Moake, R. W. Finlay and W. G. Love, *Phys. Rev.* **C21** (1980) 2147;
G. Igo, C. Whitten, W. G. Love and J. Comfort, preprint, Los Alamos (1981)
- 19) C. Mahaux, *Nucl. Phys.* **A396** (1983) 9c; and in *The interaction between medium energy nucleons in nuclei 1982*, ed. H. O. Meyer (AIP, 1983)
- 20) H. V. von Geramb, in *The interaction between medium energy nucleons in nuclei 1982*, ed. H. O. Meyer (AIP, 1983)
- 21) J. Delorme, M. Ericson, A. Figureau and N. Giraud, *Phys. Lett.* **89B** (1980) 327;
H. Toki and W. Weise, *Phys. Lett.* **92B** (1980) 265;
T. Suzuki, F. Osterfeld and J. Speth, *Phys. Lett.* **100B** (1981) 443
- 22) W. G. Love and M. A. Franey, *Phys. Rev.* **C24** (1981) 1073
- 23) S. Cohen and D. Kurath, *Nucl. Phys.* **73** (1965) 1
- 24) J. Dubach and W. C. Haxton, *Phys. Rev. Lett.* **41** (1978) 1453;
J. B. Flanz, R. S. Hicks, R. A. Lindgren, G. A. Peterson, J. Dubach and W. C. Haxton, *Phys. Rev. Lett.* **43** (1979) 1922
- 25) P. J. Siemens, *Nucl. Phys.* **A141** (1970) 225;
J. W. Negele, *Phys. Rev.* **C1** (1970) 1260;
C. Mahaux, in *The interaction between medium energy nucleons in nuclei 1982*, ed. H. O. Meyer (AIP, 1983)
- 26) A. Ingemarsson, O. Jonsson and A. Hallgren, *Nucl. Phys.* **A319** (1979) 377
- 27) K. W. Jones, private communication;
K. W. Jones, C. Glashauser, S. Nanda, R. de Swiniarski, T. Carey, W. Cornelius, J. McClelland, J. Moss, J.-L. Escudié, M. Franey, M. Gazzaly, N. Hintz, M. Haji Saeid, G. Igo, C. Whitten, W. G. Love and J. Comfort, preprint, Los Alamos (1981)
- 28) W. Reuter, G. Fricke, K. Merle and H. Miska, *Phys. Rev.* **C26** (1982) 806

- 29) H. V. von Geramb, F. A. Brieva and J. R. Rook, in *Microscopic optical potentials*, Hamburg 1978, ed. H. V. von Geramb, (Springer, Berlin, 1979)
- 30) R. R. Scheerbaum, *Nucl. Phys.* **A257** (1976) 77;
F. A. Brieva and J. R. Rook, *Nucl. Phys.* **A297** (1978) 206
- 31) B. C. Clark, S. Hama and R. L. Mercer, in *The interaction between medium energy nucleons in nuclei* 1982, ed. H. O. Meyer (AIP, 1983)
- 32) H. V. von Geramb and K. A. Amos, *Nucl. Phys.* **A163** (1971) 337;
V. A. Madsen, *Nucl. Phys.* **80** (1966) 177
- 33) R. Schaeffer and J. Raynal, unpublished
- 34) J. Raynal, in *Computing as a language of physics* (IAEA, Vienna, 1972)
- 35) W. Bauhoff, private communication
- 36) A. Mori, M. Yabe and K. Kubo, *Prog. Theor. Phys.* **68** (1982) 1217
- 37) T. A. Carey, J. M. Moss, S. J. Seestrom-Morris, A. D. Bacher, D. W. Miller, H. Nann, C. Olmer, P. Schwandt, E. J. Stephenson and W. G. Love, *Phys. Rev. Lett.* **49** (1982) 266
- 38) S. J. Seestrom-Morris, J. M. Moss, J. B. McClelland, W. D. Cornelius, T. A. Carey, N. M. Hintz, M. Gazzaly, M. A. Franey, S. Nanda and B. Aas, *Phys. Rev.* **C26** (1982) 2131